



ANNUAL REVIEWS Further

Click here to view this article's
online features:

- Download figures as PPT slides
- Navigate linked references
- Download citations
- Explore related articles
- Search keywords

High-Reynolds Number Taylor-Couette Turbulence

Siegfried Grossmann,¹ Detlef Lohse,^{2,3}
and Chao Sun^{2,4}

¹Fachbereich Physik, University of Marburg, D-35032 Marburg, Germany

²Physics of Fluids Group, Faculty of Science and Technology, J.M. Burgers Center for Fluid Dynamics, and MESA+ Institute, University of Twente, 7500 AE Enschede, Netherlands; email: d.lohse@utwente.nl, c.sun@utwente.nl

³Max Planck Institute for Dynamics and Self-Organization, 37077 Göttingen, Germany

⁴Center for Combustion Energy and Department of Thermal Engineering, Tsinghua University, 100084 Beijing, China

Annu. Rev. Fluid Mech. 2016. 48:53–80

First published online as a Review in Advance on
July 23, 2015

The *Annual Review of Fluid Mechanics* is online at
fluid.annualreviews.org

This article's doi:
10.1146/annurev-fluid-122414-034353

Copyright © 2016 by Annual Reviews.
All rights reserved

Keywords

rotating flow, fully developed turbulence, laminar and turbulent boundary layers, transport properties, quasi-Keplerian flows

Abstract

Taylor-Couette flow, the flow between two coaxial co- or counter-rotating cylinders, is one of the paradigmatic systems in the physics of fluids. The (dimensionless) control parameters are the Reynolds numbers of the inner and outer cylinders, the ratio of the cylinder radii, and the aspect ratio. One key response of the system is the torque required to retain constant angular velocities, which can be connected to the angular velocity transport through the gap. Whereas the low-Reynolds number regime was well explored in the 1980s and 1990s of the past century, in the fully turbulent regime major research activity developed only in the past decade. In this article, we review this recent progress in our understanding of fully developed Taylor-Couette turbulence from the experimental, numerical, and theoretical points of view. We focus on the parameter dependence of the global torque and on the local flow organization, including velocity profiles and boundary layers. Next, we discuss transitions between different (turbulent) flow states. We also elaborate on the relevance of this system for astrophysical disks (quasi-Keplerian flows). The review ends with a list of challenges for future research on turbulent Taylor-Couette flow.

1. INTRODUCTION

Taylor-Couette (TC) flow, the flow between two coaxial, independently rotating cylinders (as sketched in **Figure 1**), is one of the paradigmatic systems of the physics of fluids. It is, next to Rayleigh-Bénard (RB) flow (the flow in a box heated from below and cooled from above), the so-called *Drosophila* of the field, and various new concepts in fluid dynamics have been tested with these systems, such as instabilities (e.g., Taylor 1923, Coles 1965, Busse 1967, Chandrasekhar 1981, DiPrima & Swinney 1981, Drazin & Reid 1981, Donnelly 1991, Gebhardt & Grossmann 1993, Coughlin & Marcus 1996, Marques & Lopez 1997, Hristova et al. 2002, Meseguer 2002, Maretzke et al. 2014, Tuckerman 2014), nonlinear dynamics and spatiotemporal chaos (e.g., Lorenz 1963, Ahlers 1974, Pfister & Rehberg 1981, Smith & Townsend 1982, Behringer 1985, Mullin et al. 1987, Strogatz 1994), pattern formation (e.g., Andereck et al. 1986, Cross & Hohenberg 1993, Koschmieder 1993, Büchel et al. 1996, Bodenschatz et al. 2000), and turbulence (e.g., Siggia 1994, Lathrop et al. 1992b, Kadanoff 2001, Ahlers et al. 2009, Lohse & Xia 2010). From our point of

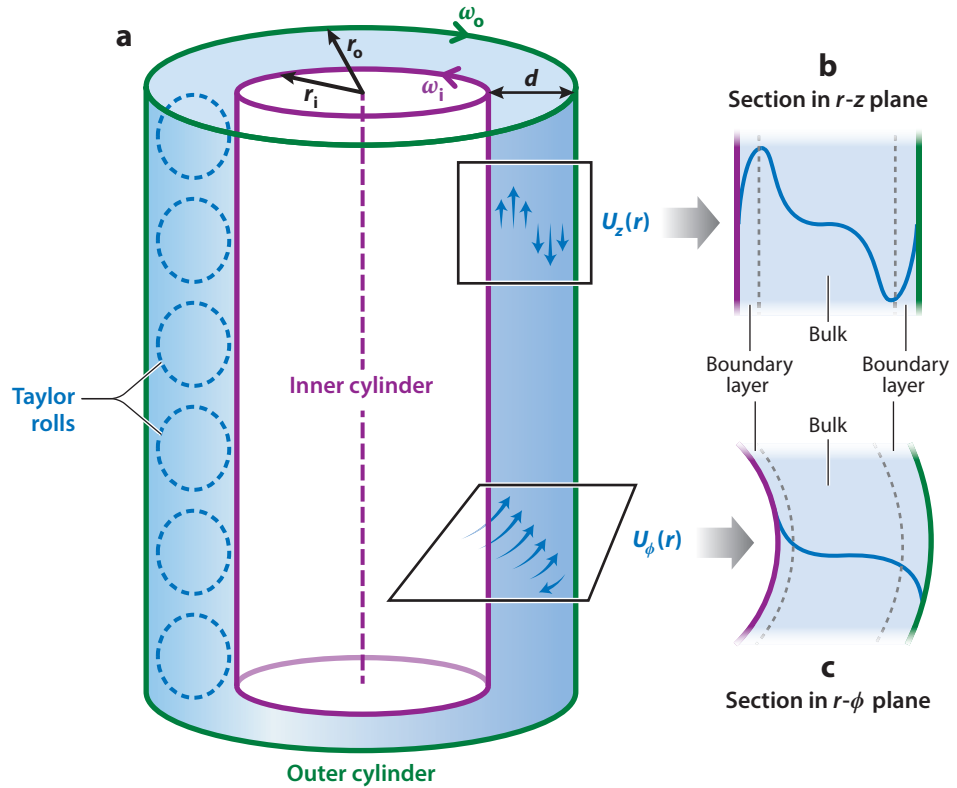


Figure 1

(a) Sketch of Taylor-Couette flow and the notation used in the present article. The inner and outer cylinder radii are r_i and r_o , respectively, and their respective angular velocities are ω_i and ω_o . The gap width is $d = r_o - r_i$. Radial distances from the origin are called r . The mean azimuthal velocity field is $U_\phi(r) = r\Omega(r)$, where $\Omega(r)$ is the angular velocity. The mean axial velocity field is $U_z(r)$, which, besides depending on r , will also depend on the axial position z . The dashed rolls indicate the Taylor roll remnants with axial and radial velocity components, which are considered to be the largest eddies of the turbulent Taylor-Couette flow. (b) The axial velocity and (c) the azimuthal velocity profiles in the boundary layers and the bulk.

view, there are several reasons why these systems are so popular: (a) They are mathematically well-defined by the Navier-Stokes equations with their respective boundary conditions. (b) For these closed systems, exact global balance relations between the respective driving and the dissipation can be derived. (c) They are experimentally accessible with high precision, given the simple geometries and high symmetries. (d) The boundaries and resulting boundary layers (BLs) play a prominent role and thus they are ideal systems to study the interaction between BLs and the bulk. (e) There is a close analogy of RB and TC flow with pipe flow (as, e.g., elaborated in Eckhardt et al. 2000, 2007a), which from a technological point of view may be the most important turbulent flow. Thus, insight into the interaction between BLs and the bulk in TC and RB turbulence will clearly also shed more light on the pipe flow problem (see, e.g., Zagarola & Smits 1998, Marusic et al. 2010, Hultmark et al. 2012).

In the 1980s, much research was done on TC flow for small Reynolds numbers, at the onset of the instabilities and slightly above, in parallel to related work for RB flow. Despite the low Reynolds numbers, up to only 1,000 or 2,000, the flow structure in this regime is extremely rich, as reflected in the phase diagram of Andereck et al. (1986), which we reproduce in **Figure 2**. In brief, TC flow is linearly stable for outer cylinder rotation and for a fixed or only slowly rotating inner cylinder. The onset of instabilities at increasing Reynolds number of the inner cylinder is caused by the driving centrifugal force and can be estimated by force balance arguments, as done by Taylor (1923) and Esser & Grossmann (1996), who generalized Rayleigh's (1917) famous stability criterion. In the unstable regime, one can observe Taylor rolls, modulated waves, spirals, and many other rich spatial and temporal flow features. For more details on this regime, readers

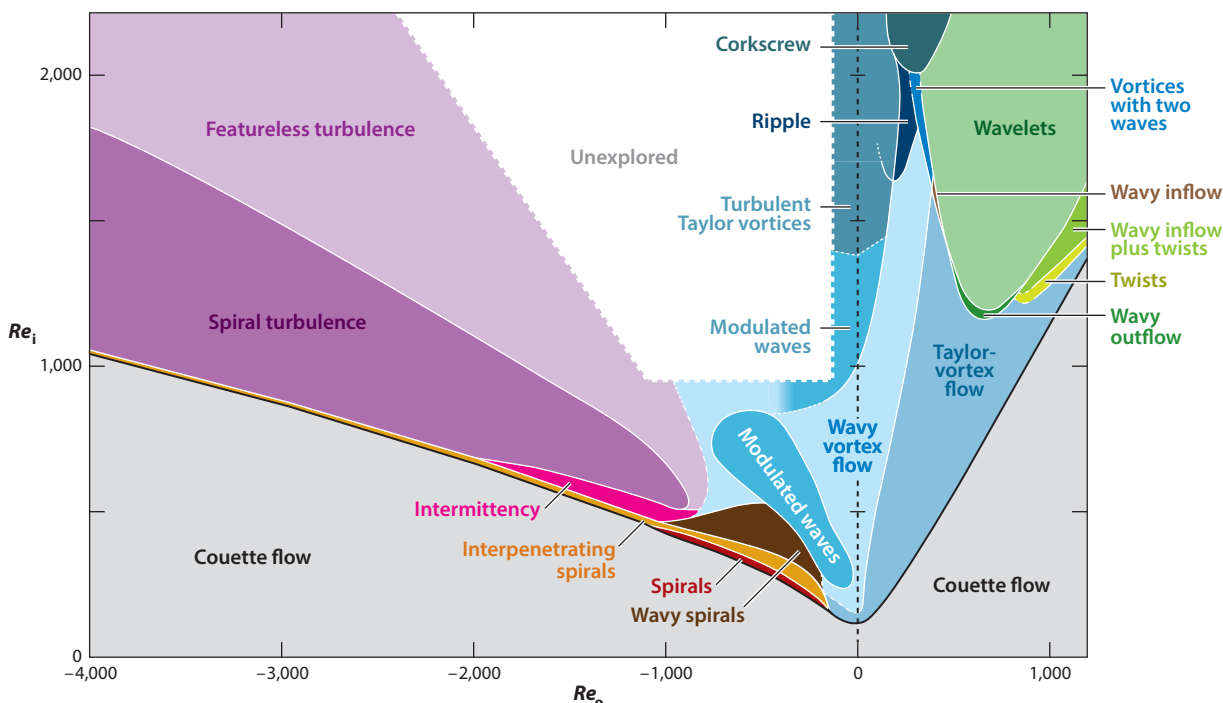


Figure 2

Observed rich flow structures in the (Re_o, Re_i) phase diagram for Taylor-Couette flow at $\eta = 0.833$. Figure taken from Andereck et al. (1986) and adapted with permission of Cambridge University Press.

are referred to the book by Chossat & Iooss (1994), the recent review by Fardin et al. (2014), and the review given in the thesis by Borrero-Echeverry (2014).

In the 1990s, the degree of turbulence for RB flow was continuously increased both experimentally with various setups and numerically with several codes (e.g., reviewed in Siggia 1994, Ahlers et al. 2009, Lohse & Xia 2010). However, there was much less activity for TC flow, with the most visible exception being the Austin-Maryland experiment by Swinney, Lathrop, and colleagues (Lathrop et al. 1992a,b; Lewis & Swinney 1999), who explored fully developed TC turbulence for pure inner cylinder rotation. For independently rotating cylinders and at the same time strongly driven turbulence, up to a few years ago the experiments by Wendt (1933) remained the most prominent ones.

This situation has changed only in the past decade, when researchers started to explore the full phase space of TC flow, that is, also for independently rotating cylinders and in the strongly turbulent regime, well beyond the onset of chaos. Many new experimental setups have been built to examine various aspects of strongly turbulent TC flow with co- and counter-rotating cylinders (Ji et al. 2006; Borrero-Echeverry et al. 2010; Ravelet et al. 2010; Paoletti & Lathrop 2011; van Gils et al. 2011a,b, 2012; van Hout & Katz 2011; Huisman et al. 2012, 2013a,b, 2014; Schartman et al. 2012; Merbold et al. 2013). Correspondingly, numerical simulations have been pushed to very high Reynolds numbers (Bilson & Bremhorst 2007; He et al. 2007; Dong 2007, 2008; Pirro & Quadrio 2008; Brauckmann & Eckhardt 2013a,b; Ostilla-Mónico et al. 2013, 2014a,b,c; Chouippe et al. 2014). **Figure 3** shows the currently explored parameter space in different representations. These phase diagrams clearly indicate that the field of high-Reynolds number TC flow has been progressing rapidly, and it is the aim of this article to review this progress.

The review is organized as follows. In Section 2, we introduce the control parameter space of TC flow and its global response. A general overview of the flow organization in different regimes of the parameter spaces is given in Section 3, together with the central idea of how to calculate the global response—namely a partitioning of the flow into a BL and the bulk part, entirely analogously to what has been done in RB flow (Grossmann & Lohse 2000, 2001, 2002, 2004). In Section 4, we report on the global response of the system. The detailed local flow organization, profiles and rolls, is described in Section 5, resulting in an explanation of when and why the system displays optimal transport properties. In that section, we also report on the occurrence of multiple turbulent states in TC flow. Whereas these first sections focus on the Rayleigh unstable regime, we touch on the Rayleigh stable regime in Section 6, owing to its relevance for astrophysical models. The review ends with a summary and an outlook on open issues.

2. CONTROL PARAMETERS AND GLOBAL RESPONSE OF TAYLOR-COUETTE FLOW

The geometric parameters describing the TC system are the inner and the outer cylinder radii r_i and r_o , respectively; the corresponding gap width $d = r_o - r_i$; and the height L of the sample (see **Figure 1**). In dimensionless form, these parameters are expressed via the radius ratio $\eta = r_i/r_o$ and the aspect ratio $\Gamma = L/d$. The system is driven through rotation of the inner and outer cylinders. This is quantified in dimensional form by the angular velocities ω_i and ω_o and in dimensionless form by the respective Reynolds numbers Re_i and Re_o , namely

$$Re_{i,o} = \frac{r_{i,o} \omega_{i,o} d}{\nu}, \quad (1)$$

where ν is the kinematic viscosity of the fluid between the cylinders. The convention is that Re_i is always positive, whereas $Re_o > 0$ stands for a corotating outer cylinder and $Re_o < 0$ for a counter-rotating outer cylinder.

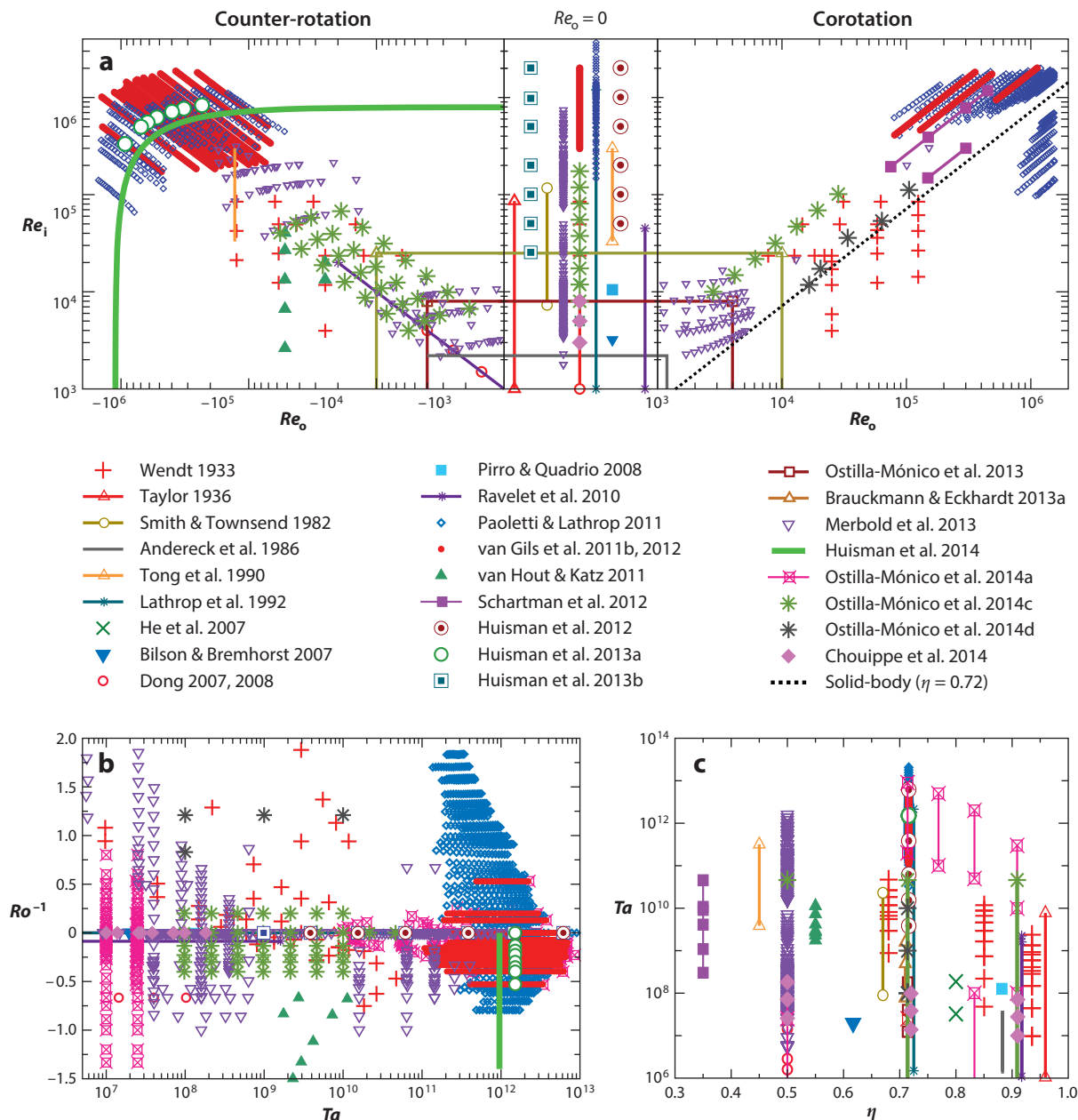


Figure 3

(a) Explored (Re_o , Re_i) parameter space of Taylor-Couette flow with independently rotating inner and outer cylinders. Shown are both experimental data (Wendt 1933; Taylor 1936; Smith & Townsend 1982; Andereck et al. 1986; Tong et al. 1990; Lathrop et al. 1992a; Ravelet et al. 2010; Paoletti & Lathrop 2011; van Gils et al. 2011b, 2012; van Hout & Katz 2011; Huisman et al. 2012, 2013a,b, 2014; Schartman et al. 2012; Merbold et al. 2013) and numerical data (He et al. 2007; Bilson & Bremhorst 2007; Dong 2007, 2008; Pirro & Quadrio 2008; Brauckmann & Eckhardt 2013a; Ostilla-Mónico et al. 2013, 2014a,c,d; Chouippe et al. 2014). The solid-body rotation line for a radius ratio $\eta = 0.72$ is included. Solid lines between markers represent a large density of experiments. (b) The (Ta , Ro^{-1}) parameter space. (c) The explored (η , Ta) parameter space.

Instead of using Re_i and Re_o , one can alternatively characterize the driving of TC flow by the Taylor number

$$Ta = \frac{(1 + \eta)^4}{64\eta^2} \frac{(r_o - r_i)^2 (r_i + r_o)^2 (\omega_i - \omega_o)^2}{v^2}, \quad (2)$$

which can be seen as the nondimensional differential rotation of the system, and the (negative) rotation ratio $a = -\omega_o/\omega_i$, with $a > 0$ for counter-rotation and $a < 0$ for corotation. As an alternative to the rotation ratio, one can use the inverse Rossby number

$$Ro^{-1} = \frac{2\omega_o d}{|\omega_i - \omega_o| r_i} = -2 \frac{1 - \eta}{\eta} \frac{a}{|1 + a|}. \quad (3)$$

The advantage of this representation is that in the coordinate system corotating with the outer cylinder, Ro^{-1} directly characterizes the strength of the driving Coriolis force, as can be seen from the underlying Navier-Stokes equation formulated in that coordinate system,

$$\frac{\partial \mathbf{u}}{\partial t} + \mathbf{u} \cdot \nabla \mathbf{u} = -\nabla p + \frac{f(\eta)}{Ta^{1/2}} \nabla^2 \mathbf{u} - Ro^{-1} \mathbf{e}_z \times \mathbf{u}, \quad (4)$$

where $f(\eta) = (1 + \eta)^3/(8\eta^2)$. The same data for the (Re_o, Re_i) parameter space of **Figure 3a** are shown in the (Ta, Ro^{-1}) parameter space in **Figure 3b**. But as shown below, the representation of the data in terms of Ro^{-1} also has disadvantages, and we use Ro^{-1} and the (negative) rotation ratio a in parallel.

The advantage of using the Taylor number rather than the Reynolds numbers is that the analogy between TC flow and RB flow is then illuminated, as we worked out in detail (Eckhardt et al. 2007b) in the spirit of the Grossmann & Lohse (2000) theory for RB flow. These authors showed, in particular, that the conserved transport quantity in TC flow is the angular velocity flux from the inner to the outer cylinder,

$$J^\omega = r^3 \langle (u_r \omega)_{A,t} - v \partial_r \langle \omega \rangle_{A,t} \rangle. \quad (5)$$

Here u_r (u_ϕ) is the radial (azimuthal) velocity, $\omega = u_\phi/r$ is the angular velocity, and $\langle \dots \rangle_{A,t}$ characterizes averaging over time and the area with constant distance from the axis. In analogy to the definition of the dimensionless heat flux in RB flow, Eckhardt et al. (2007b) defined a Nusselt number as the ratio of the angular velocity flux J^ω and its value $J_{\text{lam}}^\omega = 2vr_i^2 r_o^2 (\omega_i - \omega_o)/(r_o^2 - r_i^2)$ for the laminar case, that is,

$$Nu_\omega = J^\omega / J_{\text{lam}}^\omega. \quad (6)$$

Nu_ω is the key response parameter of the TC system. It is directly connected to the torque τ that is necessary to keep the angular velocities constant. Its dimensionless form is defined as

$$G = \frac{\tau}{2\pi \ell \rho_f v^2} = Nu_\omega \frac{J_{\text{lam}}^\omega}{v^2} = Nu_\omega G_{\text{lam}}. \quad (7)$$

Here ℓ is the height of the part of the cylinder on which the torque is measured, ρ is the density of the fluid, and G_{lam} is the dimensionless torque for the laminar case. Dubrulle & Hersant (2002) also worked out the analogy between TC and RB flow but still used the dimensionless torque G as a response parameter. Yet another possibility often used to represent the data is the friction coefficient $c_f = [(1 - \eta)^2/\pi] G/Re_i^2$ (Lathrop et al. 1992a).

Another key response parameter is the degree of turbulence of the wind in the gap of the cylinders, which measures the strength of the secondary flows—the r and z components of the velocity field (u_r and u_z). Because the time-averaged wind velocity is generally very small when the secondary flows are not stable over time (i.e., $\langle u_r \rangle \simeq 0$ and $\langle u_z \rangle \simeq 0$), the standard deviation

of the wind velocity is often used to quantify the wind Reynolds number,

$$Re_w = \frac{\sigma_{u_w}(r_o - r_i)}{v}. \quad (8)$$

σ_{u_w} can be chosen to be the standard deviation of either the radial or axial velocity.

The key issue now is to understand how the response parameters Nu_w and Re_w depend on the control parameters Ta , Ro^{-1} , and η .

3. GENERAL FLOW FEATURES WITH INCREASING DRIVING STRENGTH

Before we answer this question in Section 4, we first report the changes in the general flow features with increasing degree of turbulence. A good overview is obtained from the direct numerical simulations (DNS) of the Navier-Stokes equation of Ostilla-Mónico et al. (2014c), who significantly extended the parameter space of Andereck et al. (1986) (**Figure 2**) toward much larger Reynolds numbers (up to 10^5), as shown in **Figure 4** via phase diagrams in both the (Re_o, Re_i) and the (Ta, Ro^{-1}) representations. Note that the whole phase diagram of **Figure 2**, with all its rich structure, fits into a dot-like region in the representations of **Figure 4b**, whereas in the logarithmic representation of **Figure 4a**, it appears in the far-left part for small $Ta \lesssim 10^6$ as “lam TRs,” “lam TRs at IC,” and of course as “Rayleigh stable.”

At Taylor numbers that are still low ($Ta \sim 10^6$; see **Figure 5a**), the gap between the cylinders is filled with coherent structures (Taylor rolls, also called Taylor vortices) (e.g., reviewed in DiPrima & Swinney 1981, Tagg 1994, Fardin et al. 2014), whose length scale decreases with increasing Ta . Around $Ta \approx 3 \times 10^6$ (in the Rayleigh unstable regime), the coherence length of the structures becomes smaller than the characteristic integral length scale (the gap width d), and turbulence starts to develop in the bulk at length scales between the inner (connected to the Kolmogorov scale) and the outer length scale d . At the same time, BLs start to develop at the inner and outer cylinders, with statistical properties that differ from the bulk flow. The BLs are still of the laminar type, which—despite time dependence—can be described by the Prandtl-Blasius theory. In analogy to RB flow, we call this regime—with a turbulent bulk and BLs of the Prandtl-Blasius type—the classical regime of TC turbulence. **Figure 5b** presents a snapshot of the azimuthal velocity profile in this regime. In the turbulent bulk, depending on Ro^{-1} , either the Taylor rolls survive, or they partly survive close to the inner cylinder, or else the bulk is featureless (see **Figure 4a** and the detailed discussion in Section 5).

However, around $Ta^* \simeq 3 \times 10^8$ (for $\eta = 0.71$), the situation changes drastically, as then the BLs are sheared strongly enough to undergo a shear instability and become turbulent (i.e., of the Prandtl-von Kármán type). This regime, shown in **Figure 5c**, is called the ultimate regime of TC turbulence, again in analogy to the ultimate regime in RB flow (Kraichnan 1962, Ahlers et al. 2009, Grossmann & Lohse 2011). The typical characteristic of the turbulent BL is the approximately logarithmic velocity profile, as discussed in Section 5. Note that at this transition, the bulk flow does not change much: Depending on Ro^{-1} , it either is still featureless (for positive Ro^{-1} , meaning corotation) or features Taylor rolls—either over the full bulk area (the gap width minus the BLs) or, because of the stabilization by strong counter-rotation of the outer cylinder, only close to the inner cylinder (see **Figure 4**). In addition, the statistics of the turbulent fluctuations in the bulk change only quantitatively beyond the transition toward the ultimate regime, with the inertial regime increasing in size.

The separation of the flow domain into the bulk and BLs is analogous to the situation in RB flow. Therefore, the unifying scaling theory developed by Grossmann & Lohse (2000, 2001, 2002,

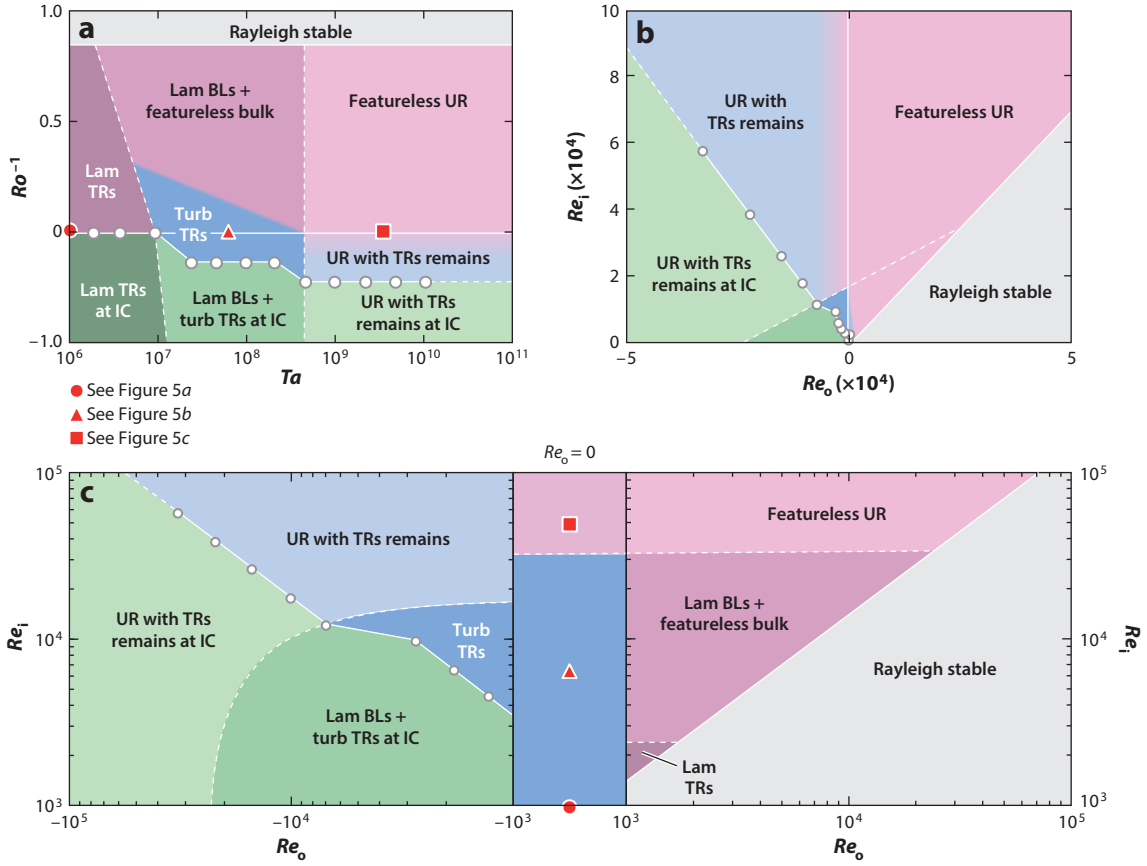


Figure 4

Different regimes in the (a) (Ta, Ro^{-1}) and (b,c) (Re_o, Re_i) phase spaces for $\eta = 0.714$, as obtained from the direct numerical simulations of Ostilla-Mónico et al. (2014c). The white circles indicate the location of optimal transport and serve as an indication of the location of the border between the corotating or weakly counter-rotating regime (blue and pink) and the strongly counter-rotating regime (green). The red dot, triangle, and square correspond to the locations of the three cases shown in Figure 5. Abbreviations: BL, boundary layer; IC, inner cylinder; TR, Taylor roll; UR, ultimate regime. Figure adapted with permission from Ostilla-Mónico et al. (2014c).

2004) for RB flow is also applicable here. This was done by Eckhardt et al. (2007b). Here we only note that this also holds for the transition to the ultimate regime and for the ultimate regime itself, both for the scaling of Nu_ω and for the profiles (Grossmann & Lohse 2011, 2012; Grossmann et al. 2014), as discussed further in the next two sections.

There is, however, a quantitative difference. In RB flow, the shear instability of the kinetic BL is only indirectly induced by the thermal driving; namely, the driving first induces a large-scale wind, which then in turn builds up the shear near the boundaries. The Rayleigh number range in the classical state is very wide (from 10^7 to 10^{14}), and the system only enters into the ultimate state at extremely high Rayleigh numbers ($Ra^* \simeq 10^{14}$ for a Prandtl number of ~ 1), which results in many challenges for experiments and numerics (Ahlers et al. 2009). Although numerous efforts have been put forward to reach this critical Rayleigh number, Ra^* , in order to study the ultimate RB turbulence, very few experiments have reached this value (e.g., Roche et al. 2010; He et al. 2012a,b; Ahlers et al. 2014).

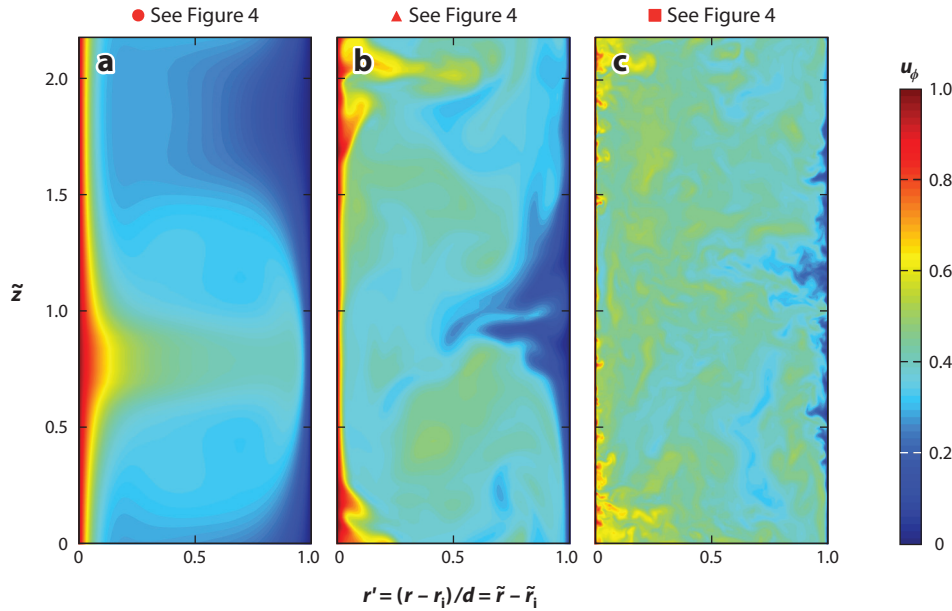


Figure 5

Snapshots of the azimuthal velocity for pure inner cylinder rotation $Ro^{-1} = 0$ and $\eta = 0.714$ as obtained from the direct numerical simulations of Ostilla-Mónico et al. (2014b). Periodic boundary conditions in the axial direction were used, and $r' = (r - r_i)/d = \tilde{r} - \tilde{r}_i$ and $\tilde{z} = z/d$. (a) $Ta = 7 \times 10^5$ (the red dot in **Figure 4**; laminar Taylor rolls), (b) $Ta = 5 \times 10^7$ (the red triangle in **Figure 4**; classical regime with boundary layers of the Prandtl-Blasius type and a turbulent bulk with Taylor rolls), and (c) $Ta = 4 \times 10^9$ (the red square in **Figure 4**; ultimate regime with turbulent boundary layers and a featureless turbulent bulk).

In contrast, in TC flow, the driving is directly through the rotating cylinders, giving rise to very large shear directly. Because the shear driving in TC flow is much more efficient than the indirect driving by heating in RB flow, the TC flow enters the ultimate regime at a much lower Ta^* , $\simeq 3 \times 10^8$ (for $\eta = 0.71$). Therefore, it is an ideal system to study turbulent flow in the ultimate regime at a wide Taylor number regime [10^8 – 10^{13} , the latter of which is what presently can be achieved in the Twente Turbulent Taylor-Couette (T³C) setup]. In the next section, we focus on the dependence of Nu_ω on the control parameters (Ta , a , and η) in both the classical (up to $Ta^* \simeq 3 \times 10^8$) and the ultimate regime (beyond $Ta \gg 3 \times 10^8$).

4. GLOBAL RESPONSE OF THE TAYLOR-COUETTE SYSTEM: Nu_ω AND Re_w

The transitions between the different regimes in the phase space are reflected in the global responses of the system. In this section, we discuss these dependences one for one.

4.1. Nu_ω and Re_w Versus Ta

The most relevant dependence may be that of Nu_ω on Ta . In a log-log plot of these quantities, it is hard to recognize the transitions. They become much more visible in so-called compensated plots, such as shown in **Figure 6a**, which plots $(Nu_\omega - 1)/Ta^{1/3}$ versus Ta , for pure inner cylinder rotation $a = 0$, for radius ratios η between 0.71 and 0.72, and for $10^4 < Ta < 10^{13}$. By plotting the

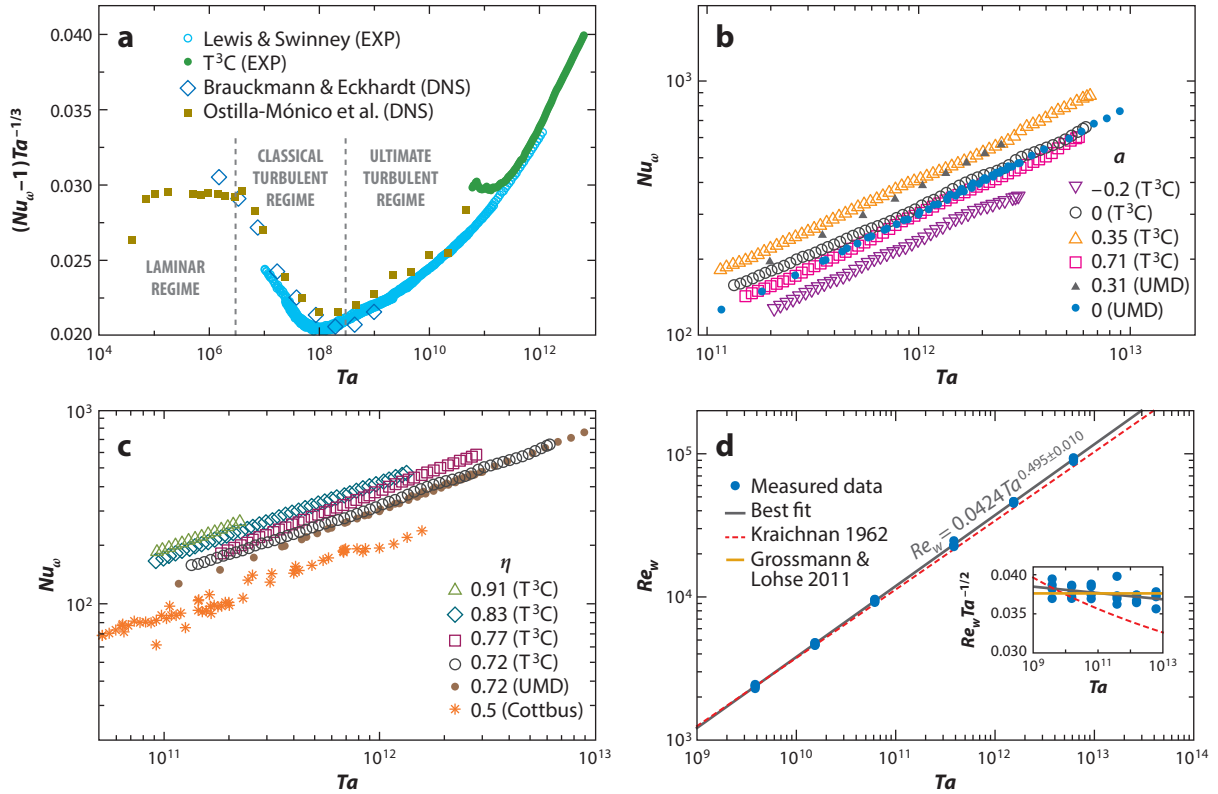


Figure 6

(a) Compensated Nu_ω versus Ta for $\eta = 0.71$ – 0.72 . The data are from experiments (EXP; $\eta = 0.72$) by Lewis & Swinney (1999) and van Gils et al. (2012) (T³C) and direct numerical simulations (DNS; $\eta = 0.71$) by Brauckmann & Eckhardt (2013a) and Ostilla-Mónico et al. (2014b). Panel *a* adapted from Ostilla-Mónico et al. (2014b). (b) Nu_ω versus Ta at various rotation ratios a , measured for $\eta \simeq 0.72$ in two different facilities, at the Twente Turbulent Taylor-Couette facility (T³C; van Gils et al. 2011b, 2012) and at the Maryland Taylor-Couette facility (UMD; Paoletti & Lathrop 2011). (c) The data on Nu_ω versus Ta for only inner cylinder rotation ($a = 0$) at various radius ratios η measured at the T³C facility (van Gils et al. 2011b, 2012), at the UMD facility (Paoletti & Lathrop 2011), and at the Cottbus Taylor-Couette facility (Merbold et al. 2013). (d) The wind Reynolds number Re_w versus Ta . The data measured at midheight at the T³C facility are shown as separate blue dots, demonstrating the quality of the reproducibility and the statistical stationarity of the measurements. The straight line is the best fit $Re_w = 0.0424Ta^{0.495 \pm 0.010}$, and the red dashed line is the Kraichnan (1962) prediction. (Inset) The compensated plot $Re_w/Ta^{1/2}$ versus Ta . The horizontal orange line is the prediction by Grossmann & Lohse (2011). Panel *d* adapted with permission from Huisman et al. (2012).

data in this compensated way, (a) the laminar case $Nu_\omega = 1$ is subtracted and (b) one focuses on the differences between the scaling exponents of the classical regime, where for $a = 0$ it is $\leq 1/3$, and the ultimate regime, where it generally is larger than $1/3$ but $\leq 1/2$, which is the theoretical upper bound (Howard 1972, Doering & Constantin 1994). As seen in **Figure 6a**, the experimental and numerical data originating from two different experimental setups and two different DNS codes agree very well: After the onset of Taylor vortices at $Ta \simeq 10^4$ and up to $Ta \simeq 3 \times 10^6$, one observes the scaling law $Nu_\omega - 1 \sim Ta^{1/3}$ for the pure laminar regime. Then the flow becomes time dependent, and for $3 \times 10^6 \lesssim Ta \lesssim 3 \times 10^8$, the effective scaling $Nu_\omega \sim Ta^\gamma$ with $\gamma < 1/3$ of the classical turbulent state is found, in correspondence with the classical effective $Nu \sim Ra^\gamma$ scaling in RB turbulence (Ahlers et al. 2009). In this regime, turbulence starts to develop in the bulk of the gap, whereas the BLs still remain of the laminar type. At some transitional Taylor

number Ta^* , which depends on η and which for $\eta = 0.71$ is $Ta^* \simeq 3 \times 10^8$, the BLs also become turbulent, and the flow undergoes a transition to the ultimate regime with an effective exponent $\gamma > 1/3$. In fact, in the Taylor number range of 10^{11} – 10^{13} , the effective exponent γ is approximately 0.39 ± 0.02 , which in this regime is consistent with the theoretical prediction of $Nu_\omega \sim Ta^{1/2} \times \log$ corrections by Kraichnan (1962) and Grossmann & Lohse (2011). Such log-correction predictions are typical for logarithmic BLs. Here they were originally derived for RB flow but can straightforwardly be translated to TC flow based on the analogies between the two systems.

How does the scaling change for co- or counter-rotation (i.e., $a \neq 0$, but fixed $\eta = 0.72$)? **Figure 6b** shows $Nu_\omega(Ta)$ measured in two different TC facilities for various a . These measurements suggest that the scaling exponent γ of $Nu_\omega \sim Ta^\gamma$ has a weak dependence on a in the Rayleigh unstable regime. And what is the dependence on the radius ratio η ? **Figure 6c** displays Nu_ω versus Ta at $a = 0$ for various η measured at three different TC facilities. Again the scaling exponent γ seems to vary only weakly. In summary, for all examined a and η values, the scaling exponent γ is found to be approximately 0.39 ± 0.03 for $10^{11} \leq Ta \leq 10^{13}$.

What about the corresponding scaling of the wind Reynolds number? For the ultimate regime (originally in RB flow), Kraichnan (1962) derived logarithmic corrections as well, namely $Re_w \sim Ta^{1/2}(\log Ta)^{-1/2}$. In contrast, Grossmann & Lohse (2011) derived a different prediction: The logarithmic corrections due to the viscous (wind) BL and the thermal (azimuthal velocity in TC) BL remarkably cancel out, resulting in the scaling $Re_w \sim Ta^{1/2}$, without any logarithmic corrections. Using high-speed particle image velocimetry, Huisman et al. (2012) directly measured the radial velocity fluctuations and extracted the wind Reynolds number as $Re_w = \sigma_{u_r}(r_o - r_i)/\nu$, where σ_{u_r} is the standard deviation of the radial velocity. The measurements shown in **Figure 6d** reveal a clear scaling of the wind Reynolds number with the Taylor number, $Re_w \sim Ta^{0.495 \pm 0.010}$, which is consistent with the prediction by Grossmann & Lohse (2011).

4.2. Nu_ω Versus a or Versus Ro^{-1}

From **Figure 6b**, we can see that the rotation ratio a hardly affects the scaling of Nu_ω versus Ta . However, this is quite different for the absolute value of Nu_ω , which does depend on a . **Figure 7a** gives a three-dimensional representation of the measured full dependence $Nu_\omega(Ta, a)$, clearly revealing the nonmonotonic dependence of Nu_ω on a , with a pronounced maximum at $a_{\text{opt}} = 0.33 \pm 0.03$ (for the radius ratio $\eta = 0.72$ of that specific experiment and for large-enough Ta), quite different from $a = 0$. This pronounced maximum of Nu_ω —also clearly seen in the projection in **Figure 7b**—reflects the optimal angular velocity transport from the inner to the outer cylinder at this angular velocity ratio. The positions of the maxima in the (Ta, Ro^{-1}) and (Re_o, Re_i) parameter spaces are marked as a connected line of white circles in **Figure 4**. For the given radius ratio, $a_{\text{opt}} = 0.33 \pm 0.03$ corresponds to $Ro_{\text{opt}}^{-1} = -0.20 \pm 0.02$. Intuitively, one might have expected that $Nu_\omega(Ta, Ro^{-1})$ has its maximum at $Ro^{-1} = 0$, i.e., $\omega_o = 0$ (pure inner cylinder rotation), as outer cylinder rotation stabilizes an increasing part of the flow volume for an increasing counter-rotation rate. This is indeed the case for small $Ta \lesssim 10^7$, as seen in **Figures 4** and **7c**, but for larger Taylor numbers, weak counter-rotation ($0 < Ro^{-1} < Ro_{\text{opt}}^{-1}$) can further enhance the angular velocity transport through intermittent turbulent bursts from the BLs (van Gils et al. 2012), although the flow is predominantly Rayleigh stable near the outer cylinder. Following Ostilla-Mónico et al. (2014c), we call the regime above the line of the maxima Ro_{opt}^{-1} in the parameter spaces of **Figure 4** the corotating or weakly counter-rotating (CWCR) regime. A reduction of the angular velocity transport only sets in below this line, in what we call the strongly counter-rotating regime (SCR). In general, the line of the maxima in parameter space reflects the

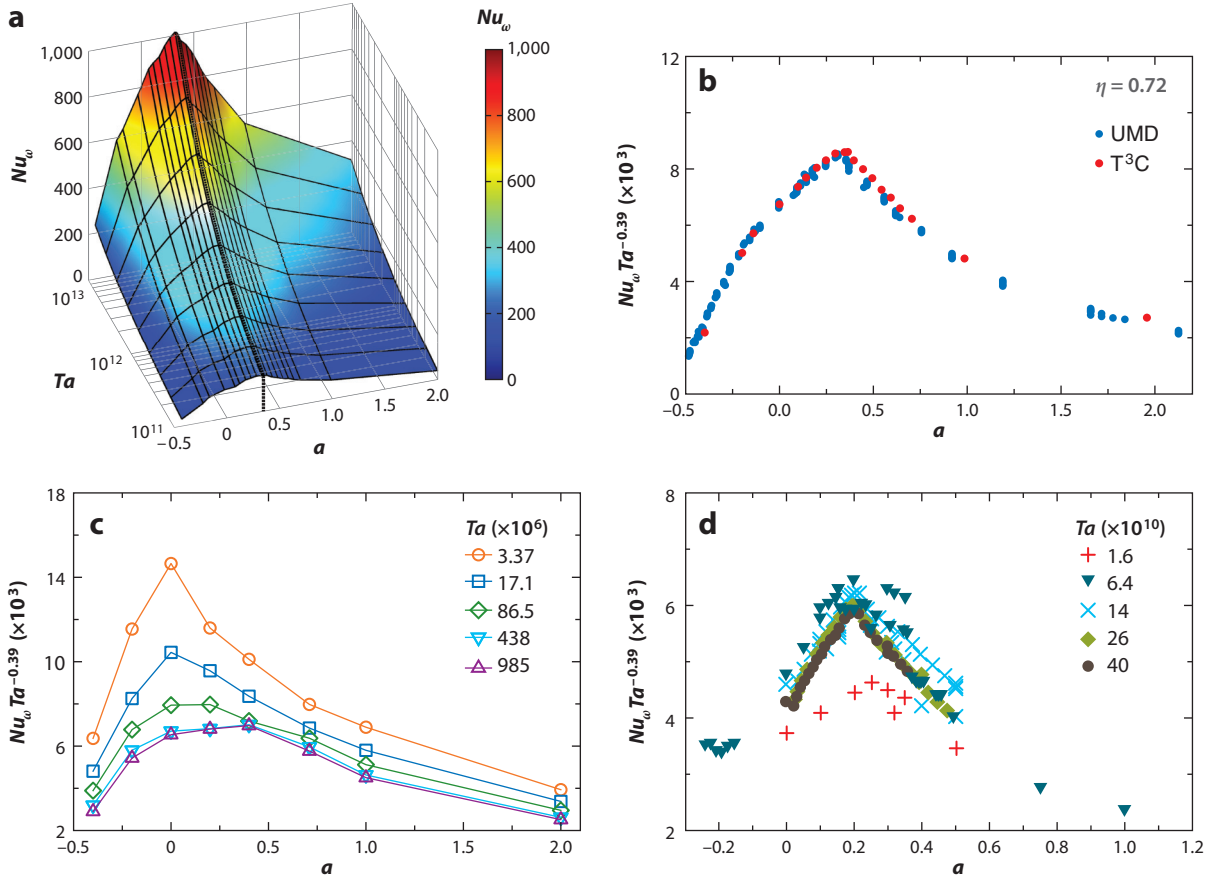


Figure 7

(a) Three-dimensional (interpolated and extrapolated) overview $Nu_\omega(Ta, a)$ of the experimental results by van Gils et al. (2012). The color and the height correspond to the Nu_ω value. Panel *a* taken with permission from van Gils et al. (2012). (b) The compensated $Nu_\omega/Ta^{0.39}$ versus a for the data measured in two different experimental facilities: the Twente Turbulent Taylor-Couette facility (T³C; van Gils et al. 2011b, 2012) and the Maryland Taylor-Couette facility (UMD; Paoletti & Lathrop 2011). The two data sets show excellent agreement. (c) Numerical and (d) experimental data for $Nu_\omega/Ta^{0.39}$ versus rotation ratio a for varying Taylor numbers at $\eta = 0.5$. Panel *c* taken from Brauckmann & Eckhardt (2013a) and reproduced by permission of Cambridge University Press, and panel *d* taken with permission from Merbold et al. (2013).

competition of destabilization by the inner cylinder rotation and stabilization by the outer cylinder rotation. This competition depends on the radius ratio η , as seen in **Figure 7c,d**, which illustrates the angular velocity transport as measured by Merbold et al. (2013) for $\eta = 0.5$, displaying a maximum around $a_{\text{opt}} = 0.20$ to 0.25 for large-enough Ta , corresponding to $Ro_{\text{opt}}^{-1} = -0.33$ to -0.4 .

In **Figure 7b–d**, we have compensated Nu_ω with $Ta^{0.39}$. This is the mean effective scaling of Nu_ω in the explored large Taylor number regime (10^9 – 10^{13}), in which $Nu_\omega(Ta, Ro^{-1}, \eta)$ factorizes into $Nu_\omega(Ta, Ro^{-1}, \eta) \sim Ta^{0.39} f(Ro^{-1}, \eta)$ or $Nu_\omega(Ta, a, \eta) \sim Ta^{0.39} f(a, \eta)$. In Section 5, we explain the dependence of the scaling function f on Ro^{-1} and η .

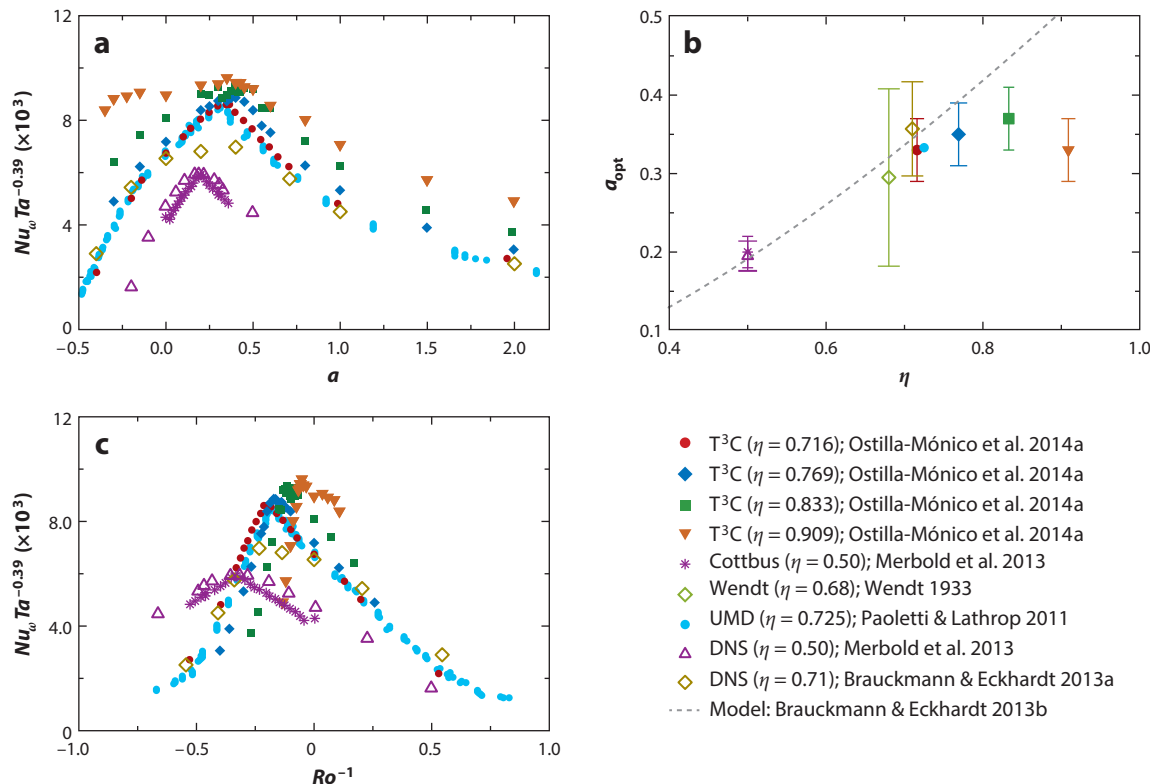


Figure 8

Radius ratio η dependence of Nu_ω : plots of $Nu_\omega/Ta^{0.39}$ versus (a) a and versus (c) Ro^{-1} from a collection of state-of-the-art data at various η . (b) a_{opt} obtained from panel a versus η . Symbols represent experimental and numerical results; the model prediction of Brauckmann & Eckhardt (2013b) is plotted as a gray dashed line. Figure adapted with permission from Ostilla-Mónico et al. (2014a). Abbreviations: Cottbus, Cottbus Taylor-Couette facility; DNS, direct numerical simulations; T³C, Twente Turbulent Taylor-Couette facility; UMD, Maryland Taylor-Couette facility.

4.3. Nu_ω Versus η

We finally report the radius ratio dependence of Nu_ω in more detail. **Figure 8a** shows $Nu_\omega/Ta^{0.39}$ as a function of a for varying values of η (0.50–0.909). Nu_ω increases with increasing η in the present parameter regime, indicating that the angular velocity transport is more efficient for a larger radius ratio η . As seen in **Figure 8a**, the shapes of the curves $Nu_\omega/Ta^{0.39}$ versus a depend strongly on η : The peak is very narrow and pronounced at low radius ratios, and the location of a_{opt} for the optimal transport can be easily identified. In contrast, for larger radius ratios, the peak of the curve becomes less steep. This suggests that the angular velocity ratio of optimal transport a_{opt} becomes less sharply defined as the radius ratio η approaches 1. As seen in **Figure 8a**, it is quite difficult to precisely identify the location of a_{opt} for $\eta = 0.909$, as the curve is almost flat for the data of $\eta = 0.909$ at $a < 0.5$.

From the curves in **Figure 8a**, we can identify a_{opt} as a function of η , which is plotted in **Figure 8b**. These data assemble state-of-the-art results on the optimal transport in high-Reynolds number TC flows. Overall, a_{opt} increases with increasing η for $\eta \lesssim 0.8$, and it seems to saturate at higher η .

The same data $Nu_\omega(a)$ in **Figure 8a** are shown in the $Nu_\omega(Ro^{-1})$ representation in **Figure 8c**, seemingly exhibiting a different trend: The steepness of the peak does not depend much on the radius ratio η . This difference in the trends in **Figure 8a,c** results from the transformation between the control parameters a and Ro^{-1} (Equation 3). As is known, Ro^{-1} takes its justification as a control parameter directly from the Navier-Stokes equations, in which it characterizes the strength of the Coriolis force. However, it is hard to compare the data of $Nu_\omega(Ro^{-1})$ for different η because Ro is defined as the ratio of the shear rate $[(\omega_i - \omega_o)/d]$ and solid-body rotation (ω_o/r_i) , which involve two different length scales (i.e., d and r_i).

Finally, we also note that the transitional Taylor number Ta^* to the ultimate state is larger at smaller radius ratios (e.g., $Ta^* \simeq 10^{10}$ for $\eta = 0.5$) (Ostilla-Mónico et al. 2014c).

5. LOCAL FLOW ORGANIZATION: PROFILES, ROLLS, AND OPTIMAL TRANSPORT

Given the general overview of the flow organization in Section 3, and after having reported the global flow response in Section 4, we now look into the profiles and the detailed flow organization. This also allows us to rationalize the dependence $f(Ro^{-1}, \eta)$ of the global transport properties reported above.

5.1. Profiles

For Taylor numbers below the threshold $Ta_c \approx 10^4$ for the onset of instabilities, the angular velocity profile in TC flow follows the classical nonvortical laminar profile (see, e.g., Landau & Lifshitz 1987),

$$\Omega_{\phi, \text{lam}}(r) = A + C/r^2, \quad A = \frac{\omega_o - \eta^2 \omega_i}{1 - \eta^2}, \quad C = \frac{(\omega_i - \omega_o)r_i^2}{1 - \eta^2}. \quad (9)$$

For larger Taylor numbers, the flow becomes time dependent, and then $\Omega(r) = \langle \omega(r) \rangle_t$ is the time-averaged angular velocity. This profile is shown in **Figure 9a** as the gray dashed line representing the laminar circular-Couette solution of the Navier-Stokes equations (for $\eta = 0.7$), in the representation $\Omega' = [\Omega(r) - \omega_o]/(\omega_i - \omega_o)$ versus $r' = (r - r_i)/(r_i - r_o)$. With increasing Taylor number, the profiles start to deviate from the nonvortical laminar one, as also shown in **Figure 9a** (for the case of zero outer cylinder rotation, $Ro^{-1} = 0$). After the onset of Taylor vortices, time dependences eventually set in, and the large-scale coherent structures break up into smaller structures. Finally, the separation between the bulk and the BLs starts to develop. As seen in **Figures 5a,b** and **9a**, between $Ta = 10^5$ and 10^7 , the profiles can be decomposed into the bulk and two BLs. The BLs can be well characterized by the Prandtl-Blasius BL theory for BLs of the laminar type, as illustrated by the black dashed lines in the figure. With further increases of the Taylor number, the BLs become increasingly thin and at approximately $Ta^* \simeq 3 \times 10^8$ finally undergo a transition to the turbulent BLs of the Prandtl-von Kármán type (see **Figure 5c**). **Figure 9a** shows the angular velocity profiles at $Ta = 10^{10}$ and 6.2×10^{12} , both clearly of the turbulent type with a logarithmic shape, as shown below.

The angular velocity profile also strongly depends on the radius ratio η , as seen from the experimental and DNS data in **Figure 9b**. The angular velocity gradient in the bulk decreases with increasing η , and the profile is almost flat in the bulk for $\eta = 0.9$. In contrast, for small $\eta = 0.5$, a large decrease of Ω' to values $\ll 0.5$ (i.e., the value in the limiting case $\eta = 1$, plane Couette flow) is observed, coinciding with a considerable angular velocity gradient.

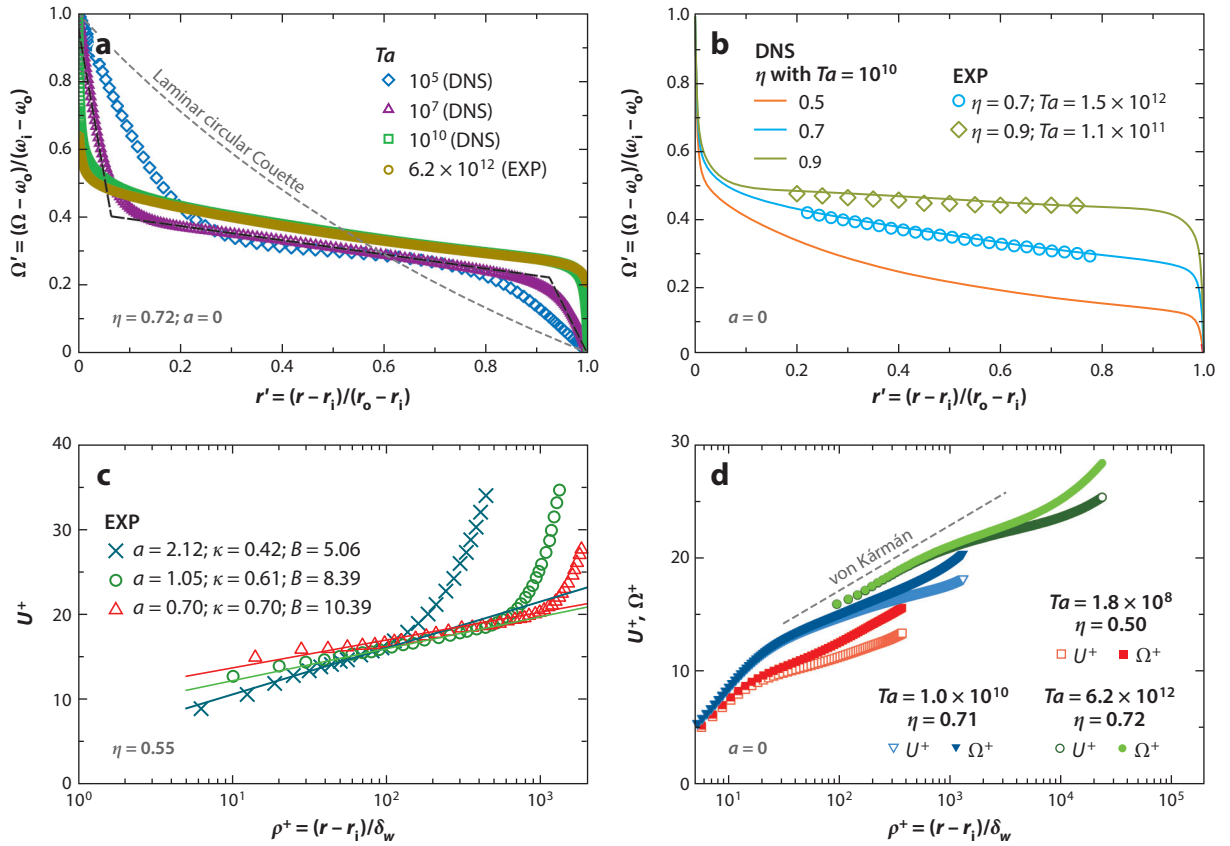


Figure 9

(a) Angular velocity profiles for varying Taylor numbers across the Taylor-Couette gap for only inner cylinder rotation at $\eta = 0.71$ [direct numerical simulations (DNS)] and 0.72 (experiments). The gray dashed line represents the exact laminar circular-Couette (nonvortical) solution of the Navier-Stokes equations. The black dashed lines are an illustration of the laminar boundary layers. Panel *a* adapted from Huisman et al. (2013b). (b) Angular velocity profiles for varying radius ratios across the Taylor-Couette gap for only inner cylinder rotation. The lines are the results from DNS, and the symbols represent the experimental data. Panel *b* adapted from Ostilla-Mónico et al. (2014a). (c) The inner cylinder azimuthal velocity profile in wall units versus the radial distance from the wall (again in wall units) at varying rotation ratios. Here $\eta = 0.55$, and the Taylor numbers are 4.9×10^9 ($a = 2.12$), 7.3×10^9 ($a = 1.05$), and 1.1×10^{10} ($a = 0.70$). Also shown as the straight lines (of the corresponding color) are the fits using Equation 10 with the corresponding values of κ and B . Panel *c* adapted with permission from van Hout & Katz (2011). (d) A log-linear plot of the inner cylinder azimuthal velocity profiles (U^+) and angular velocity profiles (Ω^+) near the inner cylinder in wall units. Experimental data at $Ta = 6.2 \times 10^{12}$ are taken from Huisman et al. (2013b), numerical data at $Ta = 1.0 \times 10^{10}$ from Ostilla-Mónico et al. (2014b), and numerical data at $Ta = 1.8 \times 10^8$ from Chouippe et al. (2014) with permission from the authors. The radial distance from the inner cylinder wall is normalized by the wall unit, i.e., $\rho^+ = (r - r_i)/\delta_{w,i}$, where $\delta_{w,i}$ is the viscous length scale for the inner cylinder boundary layer.

In the ultimate state of TC turbulence, the velocity BL is turbulent, and the profile was believed to be described by the law of the wall suggested by Prandtl and von Kármán,

$$U_\phi^+(\rho^+) = \kappa^{-1} \log \rho^+ + B. \quad (10)$$

Here κ is a generalized von Kármán constant, and $\rho = r - r_i$ or $\rho = r_o - r$ are the distances from the wall, presented in the usual wall units $\rho^+ = (r - r_i)/\delta_{w,i}$ or $\rho^+ = (r_o - r)/\delta_{w,o}$, just as $U_\phi^+ = U_\phi/u_{\tau,(i,o)}$, with $\delta_{w,(i,o)} = \nu/u_{\tau,(i,o)}$ and $u_{\tau,(i,o)} = \sqrt{\tau_{(i,o)}/\rho_f}$. Because the angular velocity flux

is conserved in the radial direction, the wall units for the outer BL are directly connected to the inner ones: $u_{\tau,i}/u_{\tau,o} = 1/\eta$ and $\delta_{w,i}/\delta_{v,o} = \eta$. In this representation, the von Kármán constants κ were found to depend on Ta and on the rotation ratio a , as shown in **Figure 9c**.

Recent work by Grossmann et al. (2014) based on the Navier-Stokes equations suggests that the log law is more appropriate for the angular velocity Ω rather than for the azimuthal velocity U_ϕ , i.e.,

$$\Omega^+(\rho^+) = \kappa^{-1} \log \rho^+ + B, \quad (11)$$

with $\Omega^+(\rho^+) \equiv [\omega_{i,o} - \Omega(\rho^+)]/\omega_{i,o}^*$ and $\omega_{i,o}^* = u_{i,o}/r_{i,o}$ for the inner (outer) cylinder BL. The difference between the angular velocity and the azimuthal velocity profiles results from the curvature. As shown in **Figure 9d**, for $\eta = 0.71$ – 0.72 , this difference only becomes notable for large wall distances near the middle of the TC gap. In contrast, for smaller radius ratio $\eta = 0.50$, the difference between the angular velocity and azimuthal velocity profiles is larger, owing to a relatively smaller r_i (**Figure 9d**). For the largest Taylor number, $Ta = 6.2 \times 10^{12}$, the angular velocity profile at ρ^+ between 100 and 1,000 roughly follows the Prandtl–von Kármán log law, with even the same von Kármán constant, $\kappa \approx 0.4$, as found for other wall-bounded turbulent flows (Smits et al. 2010, Smits & Marusic 2013). For lower Taylor numbers, the von Kármán constant κ in Equation 11 is found to be larger than 0.4 (Huisman et al. 2013b, Ostilla-Mónico et al. 2014b), presumably because the turbulent BLs are not yet fully developed for these values and because of curvature.

5.2. Rotation Ratio Dependence of Profiles and Optimal Transport

We now describe in more detail how the profiles depend on the rotation ratio a (or, alternatively, on the strength of the Coriolis force $\propto Ro^{-1}$). As seen in **Figure 10**, the angular velocity profile and flow structures in the bulk indeed strongly depend on this parameter, highlighting the effect of the Coriolis force on the flow organization. Depending on Ro^{-1} (or a), we defined two regimes in Section 3, namely a CWCR regime for $Ro^{-1} > Ro_{\text{opt}}^{-1}$ and an SCR regime for $Ro^{-1} < Ro_{\text{opt}}^{-1}$. The transition between these two regimes occurs at the value Ro_{opt}^{-1} (or a_{opt}) of the rotation ratio for which $Nu_\omega(Ro^{-1})$ is maximum.

In the CWCR regime, the Coriolis force in the Navier-Stokes equation (Equation 4) is balanced by the bulk gradient of Ω , which results in a linear relationship between Ro^{-1} and $\partial_r \Omega$ (Ostilla-Mónico et al. 2013). Here $\Omega = \langle \overline{\omega} \rangle_{z,t}$ is the time-, axially, and azimuthally averaged angular velocity. As shown for $a = -0.2$ in **Figure 10a**, the angular velocity gradient in the bulk is large, and to accommodate for this, there is a smaller Ω jump across the BLs. In this CWCR regime, the plumes ejected from the BLs can be mixed easily in the bulk. As a consequence, the large-scale structures, which essentially consist of unmixed plumes, vanish when the driving is strong enough (see, e.g., **Figure 10** at $a = -0.2$ and $Ta = 10^{10}$).

Beyond the maximum, the system enters the SCR regime; that is, the outer cylinder strongly counter-rotates and generates a Coriolis force that exceeds what the Ω gradient can balance (i.e., $Ro^{-1} < Ro_{\text{opt}}^{-1}$ or $a > a_{\text{opt}}$). The threshold value of the rotation ratio for the transition from the CWCR regime to the SCR regime corresponds to a flat Ω profile (van Gils et al. 2012, Ostilla-Mónico et al. 2014c), as shown for $a = 0.4$ in **Figure 10a**. This flat angular velocity profile in the bulk perfectly resembles RB turbulence for which, owing to the absence of a mean temperature gradient in the bulk, the whole heat transport is conveyed by the convective term (Ahlers et al. 2009). Because of the flat angular velocity profile in the bulk, there is a large Ω jump across the BLs, and thus plumes detach violently from them, strongly driving the large-scale structures. Therefore, strong large-scale structures form at $a = a_{\text{opt}}$, as shown in the middle panel of

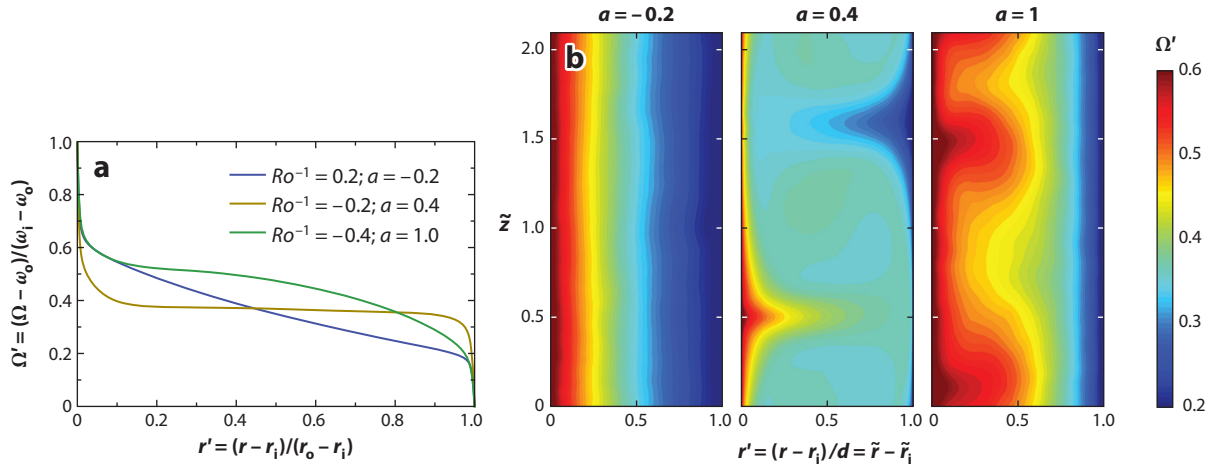


Figure 10

(a) Axially averaged angular velocity profiles at three values of Ro^{-1} (or a) for $\eta = 0.71$ and $Ta = 10^{10}$. (b) Contour plots of the azimuthally and time-averaged angular velocity field for $Ta = 10^{10}$, $\eta = 0.71$, and three values of Ro^{-1} . The left panel corresponds to $Ro^{-1} = 0.2$ ($a = -0.2$) (corotating or weakly counter-rotating regime) and shows no traces of axial dependence. Plumes detach rapidly into the bulk, in which they strongly mix and thus cannot form large-scale structures. The middle panel corresponds to $Ro^{-1} = -0.22$ ($a = 0.4$). The reduced plume mixing enables the formation of large-scale structures, and their strong signature can be seen in the averaged angular velocity field. The right panel corresponds to $Ro^{-1} = -0.4$ ($a = 1$) (strongly counter-rotating regime) and also shows some signatures of large-scale structures. However, these do not fully penetrate the gap but stop at the border to the Rayleigh-stable zones near the outer cylinder. Figure adapted with permission from Ostilla-Mónico et al. (2014c).

Figure 10b, and these strong mean circulations can be related to the optimum in the angular velocity transport Nu_ω (Brauckmann & Eckhardt 2013b, Ostilla-Mónico et al. 2014c). Ostilla-Mónico et al. (2014c) also explained the radius ratio η dependence of the angular velocity transport with the flat angular velocity profile and the persistence of Taylor rolls. Indeed, $Nu_\omega(\eta)$ seems to have its maximum close to $\eta = 1$ (plane Couette flow), at which the angular velocity profile is flat, and the rolls are most developed. However, the detailed dependence of $Nu_\omega(\eta)$ at approximately $\eta = 1$ still awaits a detailed numerical and experimental exploration.

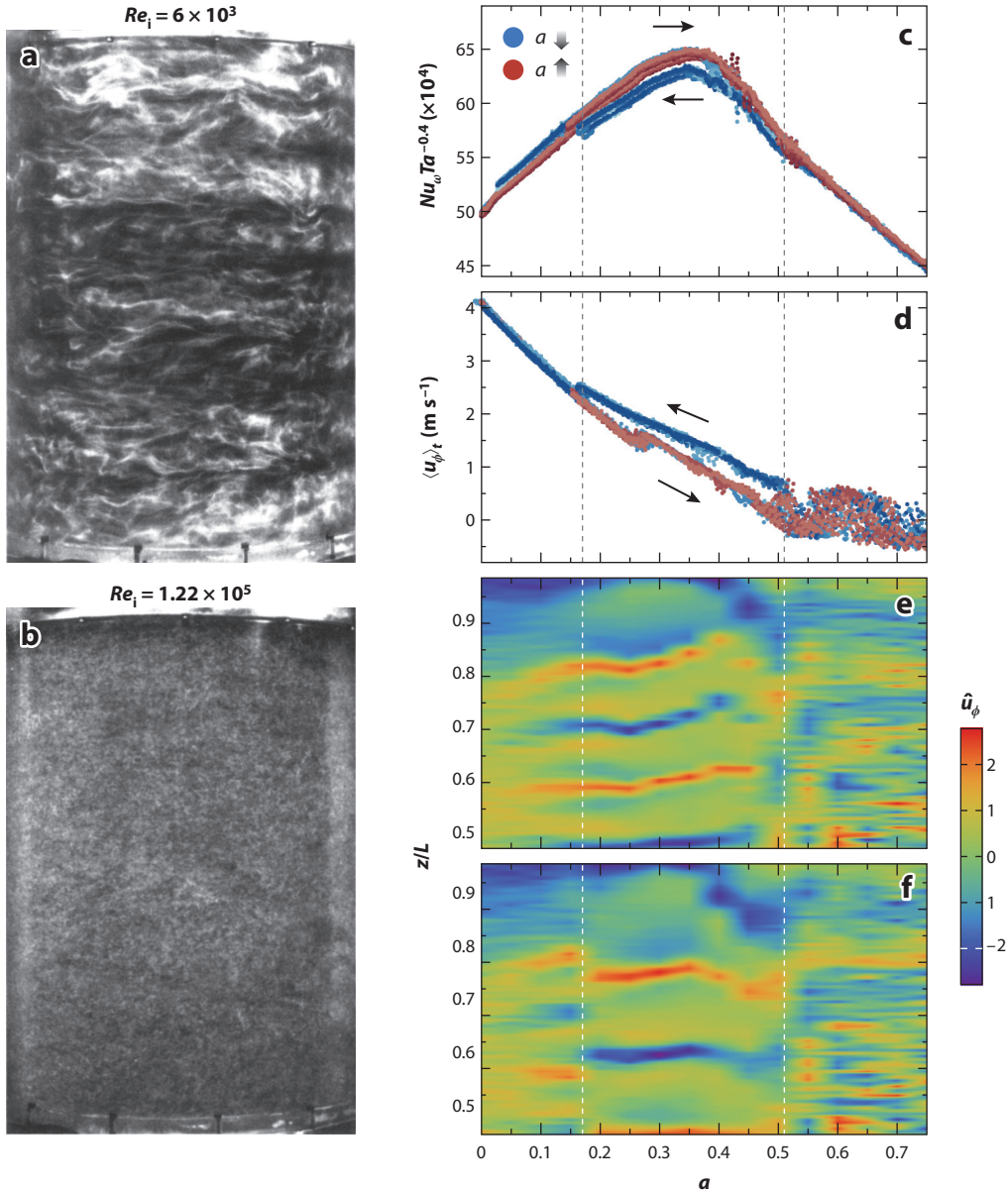
In the SCR regime, the vortices cannot fully penetrate the entire domain, owing to the insufficient strength of the Coriolis force. Near the outer cylinder, the flow is predominantly Rayleigh stable. The angular velocity is transported mainly through intermittent turbulent bursts instead of by convective transport through plumes and vortices (van Gils et al. 2012, Brauckmann & Eckhardt 2013b). In this regime, large-scale coherent rolls cannot develop in the entire gap, as shown in the right panel of **Figure 10b**. Local structures are present only in the zones close to the inner cylinder. The stabilization by the outer rotation is also clearly visible in the angular velocity profile as shown for $a = 1$ in **Figure 10a**, in which the outer BL extends deeper into the flow, and the distinction between the bulk and the BL is blurred (Ostilla-Mónico et al. 2014c).

5.3. Multiple Turbulent States and Their Connection to Taylor Rolls

The question is whether the turbulent structures seen in the DNS of Ostilla-Mónico et al. (2014c) up to $Re_{i,o} \sim 10^5$ and marked in the phase diagram shown in **Figure 4** survive in TC flows at

even higher Reynolds numbers (i.e., $Re_{i,o} \gg 10^5$), beyond what is presently numerically possible. And if so, what is the connection between the turbulent structures and global angular velocity transport at very high Reynolds numbers?

Fenstermacher et al. (1979) observed that, for increasing Reynolds numbers, the waves on top of the Taylor vortices become increasingly complex until only turbulent Taylor vortices are left. Lewis & Swinney (1999) studied the statistics of velocity fluctuations in TC flow for Re_i up to 5×10^5 for pure inner cylinder rotation and found that turbulent Taylor vortices remained at their highest Reynolds number. However, the findings of Lathrop et al. (1992a) suggest that for



pure inner cylinder rotation, the Taylor vortices are not present for Reynolds numbers beyond $Re_i = 1.2 \times 10^5$. As shown in **Figure 11a,b**, the flow structures are visible at $Re_i = 6 \times 10^3$ but seem to have disappeared at $Re_i = 1.22 \times 10^5$.

As discussed above, the flow structures in the bulk, the azimuthal velocity profile, and the optimal angular velocity transport are closely connected. It is crucial to know the characteristics of the turbulent state and the possible existence of other such states to correctly extrapolate to much higher Reynolds numbers. Kolmogorov's 1941 paradigm suggests that for strongly turbulent flows with many degrees of freedom and large fluctuations, there would only be one turbulent state as the large fluctuations would explore the entire higher-dimensional phase space. However, Huisman et al. (2014) recently observed conclusive evidence of multiple turbulent states for high-Reynolds number ($Re_{i,o} \sim 10^6$, $Ta \sim 10^{12}$) TC flow in the regime of ultimate turbulence by probing the phase space spanned by the rotation rates of the inner and outer cylinders. Furthermore, they found that the optimal transport is directly connected to the existence of large-scale coherent structures.

Figure 11c shows the compensated Nusselt number as a function of a for Huisman et al.'s (2014) measurements with increasing a and decreasing a . As can be seen, for increasing a , the torque is continuous and shows a peak at approximately $a = 0.36$, which is similar to the prior observations by van Gils et al. (2011b, 2012), Paoletti & Lathrop (2011), and Merbold et al. (2013). For decreasing a , the torque is found to be same as that with increasing a at $a > 0.51$ and $a < 0.17$. However, for $0.17 < a < 0.51$, the torque is different. For decreasing a , the system can enter another state at approximately $a = 0.51$, which is characterized by a lower torque (and thus is called low state), and at approximately $a = 0.17$, the system sharply jumps back to a higher torque state (high state). Huisman et al. (2014) repeated these experiments to check the reproducibility. For increasing a , the system always goes into the high state, whereas for decreasing a it goes to the low state (for $0.17 < a < 0.51$) with a high probability (8 out of 10).

To verify that the high and low torque states originate from two different physical flow structures, Huisman et al. (2014) measured the azimuthal velocity at half height $z = L/2$ and at the center of the gap $r = (r_i + r_o)/2$ (**Figure 11d**). The presence of multiple states in both the local measurements of the azimuthal velocity and the global measurements of the torque clearly indicates that the system can indeed be in different turbulent states, despite the very high Taylor number of $\mathcal{O}(10^{12})$ (in the ultimate regime).

To further characterize the turbulent state of the system, Huisman et al. (2014) also measured the axial dependence of the azimuthal velocity in the top half of the system at varying a for both

Figure 11

Photographs of flow states at (a) $Re_i = 6 \times 10^3$ and (b) $Re_i = 1.22 \times 10^5$, obtained using Kalliroscope flow visualization. The outer cylinder was stationary for these experiments. Eight vortices are visible in panel a but not in panel b. Panels a and b taken with permission from Lathrop et al. (1992a). (c–f) Experimental results measured at the Twente Turbulent Taylor-Couette (T^3C) facility at $Ta \simeq 10^{12}$. (c) Compensated Nu_ω as a function of a . Experiments following trajectories of decreasing a and increasing a are colored in blue and red, respectively. For decreasing a , the flow is either in a high or a low state for $0.17 < a < 0.51$, whereas for increasing a , in this regime it always is in the high state. For $a = 0.36$, the Nusselt number of the high state is 2.5% larger than that of the low state. (d) Azimuthal velocity measured at the mid-height and mid-gap as a function of a for trajectories of increasing a and decreasing a (same colors as in panel c). For the local velocity, the system bifurcates when following the trajectory of decreasing a at approximately $a = 0.51$, choosing either the high or low state for $0.17 < a < 0.51$. (e,f) Axial scans of the normalized angular velocity for varying a , following trajectories of increasing a and decreasing a , respectively. Four rolls are present in the top half of the system in panel e, whereas only three rolls are present in panel f for $0.17 < a < 0.51$. For $a < 0.17$ and $a > 0.51$, the system is in the same state, regardless of the trajectory of increasing a or decreasing a . $\hat{U}_\phi = (U_\phi - \langle U_\phi \rangle_z) / \sigma_a(u_\phi)$, where σ_a is the standard deviation of u_ϕ for each a . Panels c–f adapted with permission from Huisman et al. (2014).

the high and low states. **Figure 11e** shows the local velocity for the high state with five large minima/maxima for $a \leq 0.45$, indicating that four turbulent Taylor vortices exist in the top half of the system. For $a \geq 0.5$, the state of the system is less clear, and the system appears to jump between states (without a well-defined a dependence) (**Figure 11e**). **Figure 11f** shows the same behavior in the low state as that shown in **Figure 11e** in the high state for a outside $[0.17, 0.51]$. However, for $0.17 < a < 0.51$, it is found that the azimuthal velocity has four large minima/maxima in the low state, which is the signature of three turbulent Taylor vortices in the top half of the system.

It is surprising that multiple turbulent states exist for such high-Reynolds number TC flow in the regime of ultimate turbulence with the Reynolds number up to 10^6 . Another striking feature is that the a range, at which the stable (multiple) structures exist, corresponds to the a range for optimal torque transport, reflecting that the optimal transport is connected to the existence of the stable large-scale coherent structures.

6. FLOW IN THE QUASI-KEPLERIAN REGIME

Astrophysical disks are ubiquitous in the universe. These so-called accretion disks can be of two types: protoplanetary disks and disks around compact objects, such as white dwarfs, neutron stars, and black holes (Ji & Balbus 2013). These disks are supported almost entirely by the rotation forces, suggesting that the rotating matter follows a law similar to Kepler's for planetary motion (Ji & Balbus 2013). The orbiting matter (mostly gas) has to lose its angular momentum to move radially inward into the central object. The observed accretion rates of astrophysical disks cannot be accounted for by the transport of angular momentum resulting from pure molecular viscosity (Schartman et al. 2009, Ji & Balbus 2013). Therefore, to account for the observed transport in accretion disks, turbulence has to enter into the problem. Two possible instabilities have been proposed to account for this, namely a magnetorotational instability and a subcritical hydrodynamical instability.

Subcritical hydrodynamical instability is the reason why the TC system is relevant in this context, as it has been suggested as a model system for studying the transport behavior in accretion disks (see, e.g., Richard 2001, Dubrulle et al. 2005, Avila 2012, Ji & Balbus 2013). The astrophysical community uses different control and response parameters than those introduced in Section 2. More specifically, rather than using the Taylor number Ta (or $Re_{i,o}$) and the rotation ratio a (or the inverse Rossby number Ro^{-1}) as control parameters, that community uses a shear Reynolds number Re_s and the parameter q , which are defined through the relations (Ji et al. 2006, Paoletti et al. 2012)

$$Re_s = \frac{2}{1+\eta} |\eta Re_o - Re_i|, \quad \omega_i/\omega_o = -a = \eta^{-q}. \quad (12)$$

The q parameter is real for the corotating situation, which is the only case we consider in this section. **Figure 12a** shows the parameter space at different q values. TC flow with $q > 2$ (discussed in the previous sections) is linearly unstable at sufficiently high Reynolds numbers, owing to the centrifugal instability. In the regime $q < 2$, in which the angular momentum Ωr^2 radially increases with increasing r ($\omega_i r_i^2 < \omega_o r_o^2$), the flow is linearly stable according to the Rayleigh (1917) criterion. This includes subrotation ($\omega_i < \omega_o$), solid-body rotation ($\omega_i = \omega_o$), and super-rotation ($\omega_i > \omega_o$). The flow in the region ($\omega_i > \omega_o$ and $\omega_i r_i^2 < \omega_o r_o^2$, i.e., $0 < q < 2$) is often referred to as quasi-Keplerian flow, as it includes cylinder rotation rates ($q = 3/2$) obeying Kepler's law relating the orbital radius and period. As a response parameter, the astrophysical community uses the dimensionless turbulent viscosity β (Richard & Zahn 1999, Dubrulle et al. 2005, Hersant et al.

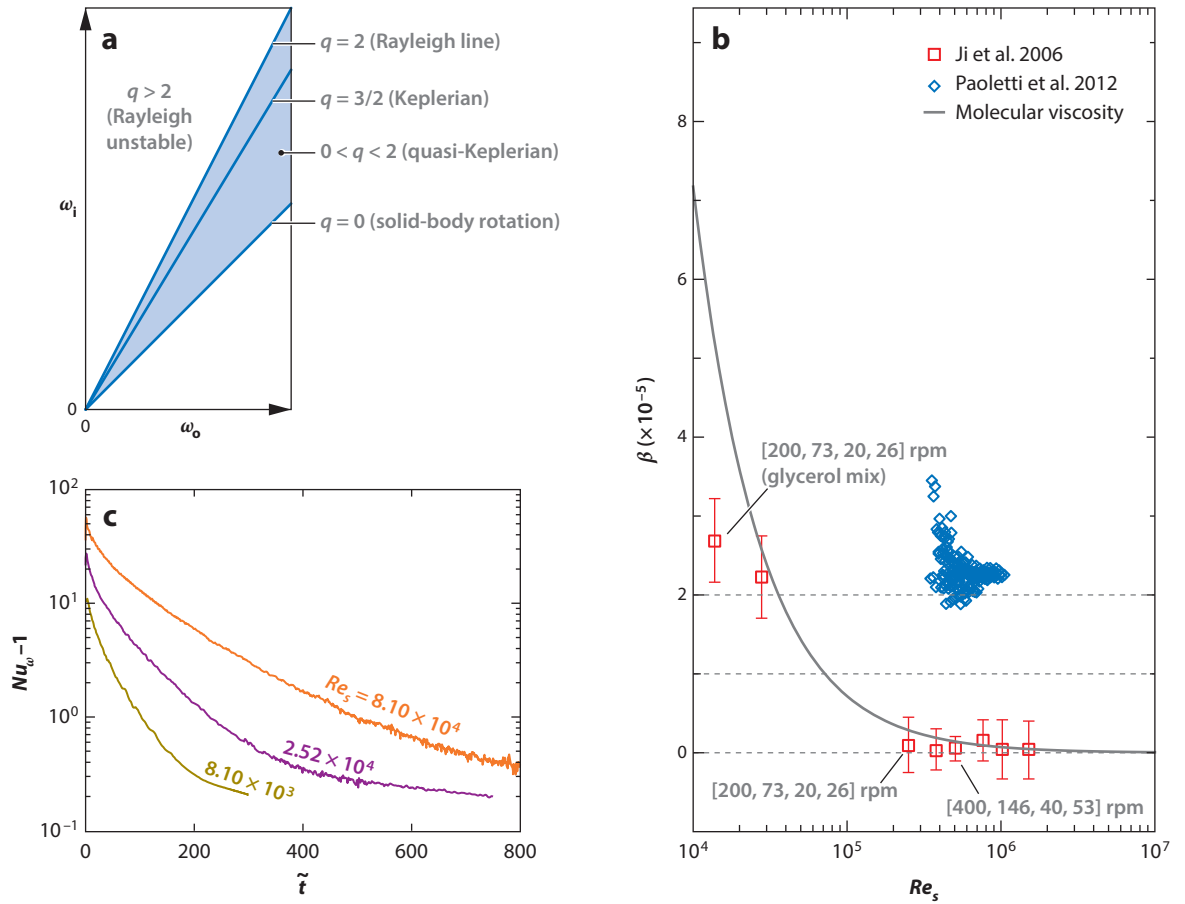


Figure 12

(a) Taylor-Couette parameter space in the corotating regime: The different regions are shown between the three lines of constant q , characterizing the Rayleigh criterion ($q = 2$), the Keplerian case ($q = 3/2$), and solid-body rotation ($q = 0$). Panel *a* adapted with permission from Nordsiek et al. (2015). (b) Dimensionless turbulent viscosity β versus the shear Reynolds number Re_s . The gray line is the molecular viscous value: $\beta_{\text{visc}} = \nu/[\bar{r}^3(\omega_i - \omega_o)/d] = \frac{16\eta(1-\eta)^2}{(1+\eta)^4} Re_s^{-1}$, where $\bar{r} = (r_o + r_i)/2$. Panel *b* adapted with permission from Ji et al. (2006) and Paoletti et al. (2012). (c) Semi-log time series of $Nu_\omega - 1$ at the inner cylinder for $Ro^{-1} = 1.22$ (implying $q = 1.5$) and three values of the shear Reynolds number: $Re_s = 8.10 \times 10^3$ (dark yellow line), $Re_s = 2.52 \times 10^4$ (purple line), and $Re_s = 8.10 \times 10^4$ (orange line). The nondimensional time in the horizontal axis has been normalized by the large-eddy turnover time of the initial state. Panel *c* adapted with permission from Ostilla-Mónico et al. (2014d).

2005) defined through

$$\beta = \frac{2(1-\eta)^4}{\pi\eta^2} \frac{G}{Re_s^2} = \frac{2(1-\eta)^4}{\pi\eta^2} \frac{Nu_\omega G_{\text{lam}}}{Re_s^2}, \quad (13)$$

rather than the dimensionless torque G or the angular velocity Nu_ω .

The key question now is whether the TC flow in the linearly stable quasi-Keplerian regime ($0 < q < 2$) can nevertheless become unstable to finite size perturbations, owing to a subcritical transition to turbulence. Indeed, despite linear stability, at large-enough Reynolds numbers, shear flow may become unstable, namely through the so-called non-normal nonlinear mechanism, as

well known from pipe flow or plane Couette flow (see, e.g., Trefethen et al. 1993, Grossmann 2000, Eckhardt et al. 2007c).

Paoletti & Lathrop (2011) and Paoletti et al. (2012) examined the flow stability by measuring the global torque as a function of Reynolds number using the Maryland Taylor-Couette facility ($\eta = 0.7245$, aspect ratio $\Gamma = 11.47$, measurements of the torque only with the central part of the inner cylinder) in the quasi-Keplerian regime. The axial boundaries (end plates) in their experiments rotated with the outer cylinder. **Figure 12b** shows the measured dimensionless turbulent viscosity β as a function of Re_s . At $Re_s \simeq 7 \times 10^5$, it is $\beta \approx 2 \times 10^{-5}$, which is much larger than the corresponding value of the laminar viscous transport, thus suggesting turbulent behavior. Extrapolating toward an astrophysical Reynolds number ($\sim 10^{13}$) by using the formula of Hersant et al. (2005), Paoletti et al. (2012) estimated that then $\beta \approx 7.5 \times 10^{-6}$, which is consistent with the values observed in disks around T Tauri stars (7×10^{-8} to 3.5×10^{-5}). However, by means of laser Doppler anemometry of the azimuthal velocity profiles in the quasi-Keplerian regime in the T³C facility, Nordsiek et al. (2015) found that the angular momentum is transported axially to the axial boundaries, suggesting that TC flow with end plates attached to the outer cylinder is an imperfect model for accretion disk flows.

Ji et al. (2006) studied the angular momentum transport in TC flow in the quasi-Keplerian regime with a different experimental setup. The radius ratio and aspect ratio were $\eta = 0.35$ and $\Gamma = 2.1$, respectively. To minimize Ekman circulation, the authors split the end plates into two rings that could independently rotate (with rotation rates of ω_3 and ω_4) with respect to the inner and outer cylinders. By carefully controlling the rotation speeds [$\omega_i, \omega_3, \omega_4, \omega_o$], they tuned the azimuthal velocity profiles in the gap to match the quasi-Keplerian flow profiles, $\Omega(r) = r^{-q}$ with $0 < q < 2$. The angular momentum transport was quantified by measuring the local angular velocity flux, $\rho r \langle u'_\theta u'_r \rangle_t$, where u'_θ and u'_r are the instantaneous velocity fluctuations in the radial and azimuthal directions, and $\langle \rangle_t$ stands for averaging over time. **Figure 12b** shows Ji et al.'s (2006) experimental results for β versus Re_s . When the end ring plates were optimized to produce Couette profiles, the values of β were found to be approximately 0.72×10^{-6} with a standard deviation of 2.7×10^{-6} at Re_s from 3×10^5 to 2×10^6 . These values are indistinguishable from the corresponding molecular viscous transport as shown with the solid line in the figure. The work by Ji et al. (2006) thus demonstrates that the axial boundaries can profoundly influence linearly stable flows and purely hydrodynamic quasi-Keplerian flows, under proper boundary conditions and at large-enough Reynolds numbers, but cannot transport angular momentum at astrophysically relevant rates.

To settle the issue of end plate effects, Avila (2012) performed DNS using both Maryland (Paoletti & Lathrop 2011) and Princeton (Ji et al. 2006) TC geometries at Re_s up to 6.5×10^3 . He found that the end ring plates do drive secondary flows that enhance the global angular momentum transport in both the Maryland and the Princeton geometries. His studies thus indicate that the current laboratory TC apparatuses designed to approximate flow profiles of accretion disks suffer from the imposed boundary conditions (end plates and finite aspect ratio). However, one would also expect that with increasing Re_s , the effect of the end plates will decrease.

To completely prevent end plate effects on the transition, Ostilla-Mónico et al. (2014d) investigated this issue numerically, using periodic boundary conditions in the axial direction at high Reynolds numbers. The shear Reynolds number they achieved in their DNS was up to 10^5 with a radius ratio of 0.7. The procedures they used for the simulations were as follows: The simulations started with a turbulent field, corresponding to a pure inner cylinder rotation in the laboratory frame ($a = 0$, $Ro^{-1} = 0$). Then the outer cylinder was switched on such that the rotation ratio was in the quasi-Keplerian regime. As shown in **Figure 12c**, the Nusselt number decreased

as a function of time down to a value corresponding to purely nonvortical laminar flow. This work thus showed not only that the TC system at $0 < q < 2$ is linearly stable in this geometry, but that even an initially turbulent flow with large shear Reynolds numbers up to 10^5 decays toward the linearly stable regime, owing to stabilizing counter-rotation. This finding is consistent with the experimental results by Edlund & Ji (2014). **Figure 12c** also shows that the decay time for turbulence becomes longer with increasing shear Reynolds number.

In summary, the present evidence indicates that the TC system in the quasi-Keplerian regime is linearly stable at shear Reynolds numbers up to $Re_s \sim 10^5 - 10^6$ (Ji et al. 2006, Edlund & Ji 2014, Ostilla-Mónico et al. 2014d). However, one cannot exclude subcritical transitions to turbulence in the quasi-Keplerian regime for TC flow at much higher shear Reynolds numbers, and it is thus necessary to examine the TC system at much higher shear Reynolds numbers.

We also note that for $q < 0$ (i.e., linearly stable but outside the quasi-Keplerian regime), subcritical transitions to turbulence may occur. For example, Borrero-Echeverry et al. (2010) studied the decay characteristics in TC flow for pure outer cylinder rotation at intermediate Reynolds numbers (up to $Re_o \sim 10^4$) and found a subcritical transition to turbulence. Burin & Czarnocki (2012) also performed experiments for pure outer cylinder rotation, finding subcritical transitions to spiral or intermittent turbulence as well, which strongly depended on the radius ratio η and the chosen end-cap configurations.

SUMMARY POINTS

1. The past decade has witnessed a tremendous extension of the experimentally and numerically studied TC parameter space toward the strongly turbulent regime, including co- and counter-rotation of the cylinders.
2. In the classical regime, the bulk is turbulent, and the BLs are of the Prandtl-Blasius (laminar) type, whereas in the ultimate regime the BLs have also become turbulent (i.e., are of the Prandtl-von Kármán type). The transition toward the ultimate regime occurs at approximately $Ta^* \simeq 3 \times 10^8$ (for $\eta = 0.71$). Because of the more efficient mechanical driving, this is much earlier than in the analogous, but thermally driven RB system, in which the transition toward the ultimate regime occurs at $Ra^* \simeq 10^{14}$.
3. In the classical regime, for pure inner cylinder rotation, the effective scaling exponent γ of $Nu_\omega \sim Ta^\gamma$ is less than $1/3$, whereas in the ultimate regime, for any rotation ratio, γ is larger than $1/3$ and follows the theoretical prediction of $Nu_\omega \sim Ta^{1/2} \times \log$ corrections.
4. At large-enough Taylor numbers, Nu_ω has a nonmonotonic dependence on the (negative) rotation ratio a with a pronounced maximum at $a_{\text{opt}} > 0$, at which the angular velocity transport is optimal. The value a_{opt} depends on η : It increases with increasing η for $\eta \lesssim 0.8$ and seems to saturate at larger η .
5. For optimal Nu_ω , the angular velocity profile is flat, and the flow displays pronounced Taylor rolls, despite the strong turbulence. The roll structure allows for the existence of multiple turbulent states with different transport and flow properties.
6. For large-enough Taylor numbers, the profiles of the BLs in the ultimate regime are reasonably well described by a log law for the angular velocity, $\Omega^+(\rho^+) = \kappa^{-1} \log \rho^+ + B$, with the well-known von Kármán constant $\kappa \approx 0.4$.

7. The current laboratory TC apparatuses designed to approximate flow profiles of accretion disks suffer from the imposed boundary conditions in the axial direction. The present experiments and numerical simulations suggest that the TC system in the quasi-Keplerian regime is linearly stable for shear Reynolds number up to $Re_s \sim 10^5 - 10^6$ and presumably beyond, for which hitherto no experiments exist. But we note that the shear Reynolds numbers relevant in astrophysical circumstellar disks are as large as 10^{13} and higher (Hersant et al. 2005).

FUTURE ISSUES

1. A rigorous theoretical understanding of the dependence of a_{opt} on η is still missing. In particular, for $\eta \rightarrow 1$, different mechanisms may be at play as compared to the situation at smaller η on which we focus above.
2. In the other limiting case, at very small radius ratios $\eta \rightarrow 0$, future investigations are needed, helping to quantitatively examine the curvature effects of the cylinders. One should also try to understand why the transitional Taylor number Ta^* to the ultimate regime becomes larger at smaller radius ratios.
3. When further increasing Ta to $Ta \gg 10^{13}$, will the large-scale coherent structures (turbulent Taylor rolls) continue to exist? If so, will multiple turbulent states still coexist, or will the fluctuation be so large that the turbulent dynamics meanders between these states?
4. With regard to the statistics of the turbulent fluctuations, structure functions, and spectra (not discussed above), Lewis & Swinney (1999) and Huisman et al. (2013a) experimentally showed that these are different as compared to homogeneous isotropic turbulence, but the reason is unknown.
5. As the TC system is closed and can be very well controlled, it is excellently suited to study multiphase turbulent flows, i.e., flows with particles, droplets, bubbles (van den Berg et al. 2005, 2007; van Gils et al. 2013), and even with vapor bubbles nucleating close to phase transitions.
6. For the same reasons, the TC system is well suited to study the interaction of turbulence with rough walls (Cadot et al. 1997, van den Berg et al. 2003), superhydrophobic walls (Srinivasan et al. 2015), and micro- and nanostructured walls, at which the structures are either of geometric or of chemical nature.

DISCLOSURE STATEMENT

The authors are not aware of any biases that might be perceived as affecting the objectivity of this review.

ACKNOWLEDGMENTS

We thank all our coworkers and colleagues for their contributions to our understanding of this great problem, for the many stimulating discussions we have had the privilege to enjoy with them

over the years, and for their valuable comments on this manuscript. We also gratefully acknowledge FOM, STW, NWO, and ERC (via an advanced grant) for financial support over the years.

LITERATURE CITED

- Ahlers G. 1974. Low temperature studies of the Rayleigh-Bénard instability and turbulence. *Phys. Rev. Lett.* 33:1185–88
- Ahlers G, Bodenschatz E, He X. 2014. Logarithmic temperature profiles of turbulent Rayleigh-Bénard convection in the classical and ultimate state for a Prandtl number of 0.8. *J. Fluid Mech.* 758:436–67
- Ahlers G, Grossmann S, Lohse D. 2009. Heat transfer and large scale dynamics in turbulent Rayleigh-Bénard convection. *Rev. Mod. Phys.* 81:503–37
- Andereck CD, Liu SS, Swinney HL. 1986. Flow regimes in a circular Couette system with independently rotating cylinders. *J. Fluid Mech.* 164:155–83
- Avila M. 2012. Stability and angular-momentum transport of fluid flows between co-rotating cylinders. *Phys. Rev. Lett.* 108:124501
- Behringer RP. 1985. Rayleigh-Bénard convection and turbulence in liquid helium. *Rev. Mod. Phys.* 57:657–87
- Bilson M, Bremhorst K. 2007. Direct numerical simulation of turbulent Taylor-Couette flow. *J. Fluid Mech.* 579:227–70
- Bodenschatz E, Pesch W, Ahlers G. 2000. Recent developments in Rayleigh-Bénard convection. *Annu. Rev. Fluid Mech.* 32:709–78
- Borrero-Echeverry D. 2014. *Subcritical transition to turbulence in Taylor-Couette flow*. PhD Thesis, Georgia Inst. Technol., Atlanta
- Borrero-Echeverry D, Schatz MF, Tagg R. 2010. Transient turbulence in Taylor-Couette flow. *Phys. Rev. E* 81:025301
- Brauckmann HJ, Eckhardt B. 2013a. Direct numerical simulations of local and global torque in Taylor-Couette flow up to $Re = 30\,000$. *J. Fluid Mech.* 718:398–427
- Brauckmann HJ, Eckhardt B. 2013b. Intermittent boundary layers and torque maxima in Taylor-Couette flow. *Phys. Rev. E* 87:033004
- Büchel P, Lücke M, Roth D, Schmitz R. 1996. Pattern selection in the absolutely unstable regime as a nonlinear eigenvalue problem: Taylor vortices in axial flow. *Phys. Rev. E* 53:4764–77
- Burin MJ, Czarnocki CJ. 2012. Subcritical transition and spiral turbulence in circular Couette flow. *J. Fluid Mech.* 709:106–22
- Busse FH. 1967. The stability of finite amplitude cellular convection and its relation to an extremum principle. *J. Fluid Mech.* 30:625–49
- Cadot O, Couder Y, Daerr A, Douady S, Tsinober A. 1997. Energy injection in closed turbulent flows: stirring through boundary layers versus inertial stirring. *Phys. Rev. E* 56:427–33
- Chandrasekhar S. 1981. *Hydrodynamic and Hydromagnetic Stability*. New York: Dover
- Chossat P, Iooss G. 1994. *The Couette-Taylor Problem*. New York: Springer
- Chouippe A, Climent E, Legendre D, Gabillet C. 2014. Numerical simulation of bubble dispersion in turbulent Taylor-Couette flow. *Phys. Fluids* 26:043304
- Coles D. 1965. Transition in circular Couette flow. *J. Fluid Mech.* 21:385–425
- Coughlin K, Marcus PS. 1996. Turbulent bursts in Couette-Taylor flow. *Phys. Rev. Lett.* 77:2214–17
- Cross MC, Hohenberg PC. 1993. Pattern formation outside of equilibrium. *Rev. Mod. Phys.* 65:851–1112
- DiPrima RC, Swinney HL. 1981. Instabilities and transition in flow between concentric rotating cylinders. In *Hydrodynamic Instabilities and the Transition to Turbulence*, ed. HL Swinney, JP Gollub, pp. 139–80. New York: Springer
- Doering C, Constantin P. 1994. Variational bounds on energy dissipation in incompressible flow: shear flow. *Phys. Rev. E* 49:4087–99
- Dong S. 2007. Direct numerical simulation of turbulent Taylor-Couette flow. *J. Fluid Mech.* 587:373–93
- Dong S. 2008. Turbulent flow between counter-rotating concentric cylinders: a direct numerical simulation study. *J. Fluid Mech.* 615:371–99
- Donnelly RJ. 1991. Taylor-Couette flow: the early days. *Phys. Today* 44(11):32–39

- Drazin P, Reid WH. 1981. *Hydrodynamic Stability*. Cambridge, UK: Cambridge Univ. Press
- Dubrulle B, Dauchot O, Daviaud F, Longgaretti PY, Richard D, Zahn JP. 2005. Stability and turbulent transport in Taylor-Couette flow from analysis of experimental data. *Phys. Fluids* 17:095103
- Dubrulle B, Hersant F. 2002. Momentum transport and torque scaling in Taylor-Couette flow from an analogy with turbulent convection. *Eur. Phys. J. B* 26:379–86
- Eckhardt B, Grossmann S, Lohse D. 2000. Scaling of global momentum transport in Taylor-Couette and pipe flow. *Eur. Phys. J. B* 18:541–44
- Eckhardt B, Grossmann S, Lohse D. 2007a. Fluxes and energy dissipation in thermal convection and shear flows. *Europhys. Lett.* 78:24001
- Eckhardt B, Grossmann S, Lohse D. 2007b. Torque scaling in turbulent Taylor-Couette flow between independently rotating cylinders. *J. Fluid Mech.* 581:221–50
- Eckhardt B, Schneider T, Hof B, Westerweel J. 2007c. Turbulence transition in pipe flow. *Annu. Rev. Fluid Mech.* 39:447–68
- Edlund EM, Ji H. 2014. Nonlinear stability of laboratory quasi-Keplerian flows. *Phys. Rev. E* 89:021004
- Esser A, Grossmann S. 1996. Analytic expression for Taylor-Couette stability boundary. *Phys. Fluids* 8:1814–19
- Hersant F, Dubrulle B, Huré J-M. 2005. Turbulence in circumstellar disks. *Astron. Astrophys.* 429:531–42
- Fardin MA, Perge C, Taberlet N. 2014. “The hydrogen atom of fluid dynamics”: introduction to the Taylor-Couette flow for soft matter scientists. *Soft Matter* 10:3523–35
- Fenstermacher PR, Swinney HL, Gollub JP. 1979. Dynamical instabilities and the transition to chaotic Taylor vortex flow. *J. Fluid Mech.* 94:103–28
- Gebhardt T, Grossmann S. 1993. The Taylor-Couette eigenvalue problem with independently rotating cylinders. *Z. Phys. B* 90:475–90
- Grossmann S. 2000. The onset of shear flow turbulence. *Rev. Mod. Phys.* 72:603–18
- Grossmann S, Lohse D. 2000. Scaling in thermal convection: a unifying view. *J. Fluid. Mech.* 407:27–56
- Grossmann S, Lohse D. 2001. Thermal convection for large Prandtl number. *Phys. Rev. Lett.* 86:3316–19
- Grossmann S, Lohse D. 2002. Prandtl and Rayleigh number dependence of the Reynolds number in turbulent thermal convection. *Phys. Rev. E* 66:016305
- Grossmann S, Lohse D. 2004. Fluctuations in turbulent Rayleigh-Bénard convection: the role of plumes. *Phys. Fluids* 16:4462–72
- Grossmann S, Lohse D. 2011. Multiple scaling in the ultimate regime of thermal convection. *Phys. Fluids* 23:045108
- Grossmann S, Lohse D. 2012. Logarithmic temperature profiles in the ultimate regime of thermal convection. *Phys. Fluids* 24:125103
- Grossmann S, Lohse D, Sun C. 2014. Velocity profiles in strongly turbulent Taylor-Couette flow. *Phys. Fluids* 26:025114
- He W, Tanahashi M, Miyauchi T. 2007. Direct numerical simulation of turbulent Taylor-Couette flow with high Reynolds number. In *Advances in Turbulence XI: Proceedings of the 11th EUROMECH European Turbulence Conference, June 25–28, 2007, Porto, Portugal*, ed. JMLM Palma, A Silva Lopes, pp. 215–17. New York: Springer
- He X, Funfschilling D, Bodenschatz E, Ahlers G. 2012a. Heat transport by turbulent Rayleigh-Bénard convection for $Pr = 0.8$ and $4 \times 10^{11} \lesssim Ra \lesssim 2 \times 10^{14}$: ultimate-state transition for aspect ratio $\Gamma = 1.00$. *New J. Phys.* 14:063030
- He X, Funfschilling D, Nobach H, Bodenschatz E, Ahlers G. 2012b. Transition to the ultimate state of turbulent Rayleigh-Bénard convection. *Phys. Rev. Lett.* 108:024502
- Howard LN. 1972. Bounds on flow quantities. *Annu. Rev. Fluid. Mech.* 4:473–94
- Hristova H, Roch S, Schmid P, Tuckerman L. 2002. Transient growth in Taylor-Couette flow. *Phys. Fluids* 14:3475–84
- Huisman SG, Lohse D, Sun C. 2013a. Statistics of turbulent fluctuations in counter-rotating Taylor-Couette flows. *Phys. Rev. E* 88:063001
- Huisman SG, Scharnowski S, Cierpka C, Kähler C, Lohse D, Sun C. 2013b. Logarithmic boundary layers in strong Taylor-Couette turbulence. *Phys. Rev. Lett.* 110:264501
- Huisman SG, van der Veen RCA, Sun C, Lohse D. 2014. Multiple states in highly turbulent Taylor-Couette flow. *Nat. Commun.* 5:3820

- Huisman SG, van Gils DPM, Grossmann S, Sun C, Lohse D. 2012. Ultimate turbulent Taylor-Couette flow. *Phys. Rev. Lett.* 108:024501
- Hultmark M, Vallikivi M, Bailey SCC, Smits AJ. 2012. Turbulent pipe flow at extreme Reynolds numbers. *Phys. Rev. Lett.* 108:094501
- Ji H, Balbus S. 2013. Angular momentum transport in astrophysics and in the lab. *Phys. Today* 66(8):27
- Ji H, Burin M, Scharfman E, Goodman J. 2006. Hydrodynamic turbulence cannot transport angular momentum effectively in astrophysical disks. *Nature* 444:343–46
- Kadanoff LP. 2001. Turbulent heat flow: structures and scaling. *Phys. Today* 54:34–39
- Koschmieder EL. 1993. *Bénard Cells and Taylor Vortices*. Cambridge, UK: Cambridge Univ. Press
- Kraichnan RH. 1962. Turbulent thermal convection at arbitrary Prandtl number. *Phys. Fluids* 5:1374–89
- Landau LD, Lifshitz EM. 1987. *Fluid Mechanics*. Oxford: Pergamon
- Lathrop DP, Fineberg J, Swinney HS. 1992a. Transition to shear-driven turbulence in Couette-Taylor flow. *Phys. Rev. A* 46:6390–405
- Lathrop DP, Fineberg J, Swinney HS. 1992b. Turbulent flow between concentric rotating cylinders at large Reynolds numbers. *Phys. Rev. Lett.* 68:1515–18
- Lewis GS, Swinney HL. 1999. Velocity structure functions, scaling, and transitions in high-Reynolds-number Couette-Taylor flow. *Phys. Rev. E* 59:5457–67
- Lohse D, Xia KQ. 2010. Small-scale properties of turbulent Rayleigh-Bénard convection. *Annu. Rev. Fluid Mech.* 42:335–64
- Lorenz EN. 1963. Deterministic nonperiodic flow. *J. Atmos. Sci.* 20:130–41
- Maretzke S, Hof B, Avila M. 2014. Transient growth in linearly stable Taylor-Couette flows. *J. Fluid Mech.* 742:254–90
- Marques F, Lopez J. 1997. Taylor-Couette flow with axial oscillations of the inner cylinder: Floquet analysis of the basic flow. *J. Fluid Mech.* 348:153–75
- Marusic I, McKeon BJ, Monkewitz PA, Nagib HM, Smits AJ, Sreenivasan KR. 2010. Wall-bounded turbulent flows at high Reynolds numbers: recent advances and key issues. *Phys. Fluids* 22:065103
- Merbold S, Brauckmann HJ, Egbers C. 2013. Torque measurements and numerical determination in differentially rotating wide gap Taylor-Couette flow. *Phys. Rev. E* 87:023014
- Meseguer A. 2002. Energy transient growth in the Taylor-Couette problem. *Phys. Fluids* 14:1655–60
- Mullin T, Cliffe KA, Pfister G. 1987. Unusual time-dependent phenomena in Taylor-Couette flow at moderately low Reynolds numbers. *Phys. Rev. Lett.* 58:2212–15
- Nordsiek F, Huisman SG, van der Veen RCA, Sun C, Lohse D, Lathrop DP. 2015. Azimuthal velocity profiles in Rayleigh-stable Taylor-Couette flow and implied axial angular momentum transport. *J. Fluid Mech.* 744:342–62
- Ostilla-Mónico R, Huisman SG, Jannink TJG, Van Gils DPM, Verzicco R, et al. 2014a. Optimal Taylor-Couette flow: radius ratio dependence. *J. Fluid Mech.* 747:1–29
- Ostilla-Mónico R, Stevens RJAM, Grossmann S, Verzicco R, Lohse D. 2013. Optimal Taylor-Couette flow: direct numerical simulations. *J. Fluid Mech.* 719:14–46
- Ostilla-Mónico R, van der Poel EP, Verzicco R, Grossmann S, Lohse D. 2014b. Boundary layer dynamics at the transition between the classical and the ultimate regime of Taylor-Couette flow. *Phys. Fluids* 26:015114
- Ostilla-Mónico R, van der Poel EP, Verzicco R, Grossmann S, Lohse D. 2014c. Exploring the phase diagram of fully turbulent Taylor-Couette flow. *J. Fluid Mech.* 761:1–26
- Ostilla-Mónico R, Verzicco R, Grossmann S, Lohse D. 2014d. Turbulence decay towards the linearly stable regime of Taylor-Couette flow. *J. Fluid Mech.* 748:R3
- Paoletti MS, Lathrop DP. 2011. Angular momentum transport in turbulent flow between independently rotating cylinders. *Phys. Rev. Lett.* 106:024501
- Paoletti MS, van Gils DPM, Dubrulle B, Sun C, Lohse D, Lathrop DP. 2012. Angular momentum transport and turbulence in laboratory models of Keplerian flows. *Astron. Astrophys.* 547:A64
- Pfister G, Rehberg I. 1981. Space dependent order parameter in circular Couette flow transitions. *Phys. Lett.* 83:19–22
- Pirro D, Quadrio M. 2008. Direct numerical simulation of turbulent Taylor-Couette flow. *Eur. J. Mech. B Fluids* 27:552–66

- Ravelet F, Delfos R, Westerweel J. 2010. Influence of global rotation and Reynolds number on the large-scale features of a turbulent Taylor–Couette flow. *Phys. Fluids* 22:055103
- Rayleigh L. 1917. On the dynamics of revolving fluids. *Proc. R. Soc. Lond. A* 93:148–54
- Richard D. 2001. *Instabilités hydrodynamiques dans les écoulements en rotation différentielle*. PhD Thesis, Univ. Paris-Diderot
- Richard D, Zahn J. 1999. Turbulence in differentially rotating flows: what can be learned from the Couette–Taylor experiment. *Astron. Astrophys.* 347:734–38
- Roche PE, Gauthier G, Kaiser R, Salort J. 2010. On the triggering of the ultimate regime of convection. *New J. Phys.* 12:085014
- Schartman E, Ji H, Burin MJ. 2009. Development of a Couette–Taylor flow device with active minimization of secondary circulation. *Rev. Sci. Instrum.* 80:024501
- Schartman E, Ji H, Burin MJ, Goodman J. 2012. Stability of quasi-Keplerian shear flow in a laboratory experiment. *Astron. Astrophys.* 543:A94
- Siggia ED. 1994. High Rayleigh number convection. *Annu. Rev. Fluid Mech.* 26:137–68
- Smith GP, Townsend AA. 1982. Turbulent Couette flow between concentric cylinders at large Taylor numbers. *J. Fluid Mech.* 123:187–217
- Smits AJ, Marusic I. 2013. Wall-bounded turbulence. *Phys. Today* 66:25–30
- Smits AJ, McKeon BJ, Marusic I. 2010. High-Reynolds number wall turbulence. *Annu. Rev. Fluid Mech.* 43:353–75
- Srinivasan S, Kleingartner JA, Gilbert JB, Cohen RE, Milne AJB, McKinley GH. 2015. Sustainable drag reduction in turbulent Taylor–Couette flows by depositing sprayable superhydrophobic surfaces. *Phys. Rev. Lett.* 114:014501
- Strogatz SH. 1994. *Nonlinear Dynamics and Chaos*. New York: Perseus
- Tagg R. 1994. The Couette–Taylor problem. *Nonlinear Sci. Today* 4(3):1–25
- Taylor GI. 1923. Stability of a viscous liquid contained between two rotating cylinders. *Philos. Trans. R. Soc. A* 223:289–343
- Taylor GI. 1936. Fluid friction between rotating cylinders. *Proc. R. Soc. Lond. A* 157:546–64
- Tong P, Goldburg WI, Huang JS, Witten TA. 1990. Anisotropy in turbulent drag reduction. *Phys. Rev. Lett.* 65:2780–83
- Trefethen L, Trefethen A, Reddy S, Driscoll T. 1993. Hydrodynamic stability without eigenvalues. *Science* 261:578–84
- Tuckerman LS. 2014. Taylor vortices versus Taylor columns. *J. Fluid Mech.* 750:1–4
- van den Berg TH, Doering C, Lohse D, Lathrop D. 2003. Smooth and rough boundaries in turbulent Taylor–Couette flow. *Phys. Rev. E* 68:036307
- van den Berg TH, Luther S, Lathrop DP, Lohse D. 2005. Drag reduction in bubbly Taylor–Couette turbulence. *Phys. Rev. Lett.* 94:044501
- van den Berg TH, van Gils DPM, Lathrop DP, Lohse D. 2007. Bubbly turbulent drag reduction is a boundary layer effect. *Phys. Rev. Lett.* 98:084501
- van Gils DPM, Bruggert GW, Lathrop DP, Sun C, Lohse D. 2011a. The Twente turbulent Taylor–Couette (T³C) facility: strongly turbulent (multi-phase) flow between independently rotating cylinders. *Rev. Sci. Instrum.* 82:025105
- van Gils DPM, Huisman SG, Bruggert GW, Sun C, Lohse D. 2011b. Torque scaling in turbulent Taylor–Couette flow with co- and counter-rotating cylinders. *Phys. Rev. Lett.* 106:024502
- van Gils DPM, Huisman SG, Grossmann S, Sun C, Lohse D. 2012. Optimal Taylor–Couette turbulence. *J. Fluid Mech.* 706:118–49
- van Gils DPM, Narezo-Guzman D, Sun C, Lohse D. 2013. The importance of bubble deformability for strong drag reduction in bubbly turbulent Taylor–Couette flow. *J. Fluid Mech.* 722:317–47
- van Hout R, Katz J. 2011. Measurements of mean flow and turbulence characteristics in high-Reynolds number counter-rotating Taylor–Couette flow. *Phys. Fluids* 23:105102
- Wendt F. 1933. Turbulente Strömungen zwischen zwei rotierenden Zylindern. *Ingenieurs-Archiv* 4:577–95
- Zagarola MV, Smits AJ. 1998. Mean-flow scaling of turbulent pipe flow. *J. Fluid Mech.* 373:33–79



Contents

Biomimetic Survival Hydrodynamics and Flow Sensing <i>Michael S. Triantafyllou, Gabriel D. Weymouth, and Jianmin Miao</i>	1
Motion and Deformation of Elastic Capsules and Vesicles in Flow <i>Dominique Barthès-Biesel</i>	25
High-Reynolds Number Taylor-Couette Turbulence <i>Siegfried Grossmann, Detlef Lohse, and Chao Sun</i>	53
Shear Banding of Complex Fluids <i>Thibaut Divoux, Marc A. Fardin, Sebastien Manneville, and Sandra Lerouge</i>	81
Bacterial Hydrodynamics <i>Eric Lauga</i>	105
Quadrant Analysis in Turbulence Research: History and Evolution <i>James M. Wallace</i>	131
Modeling of Fine-Particle Formation in Turbulent Flames <i>Venkat Raman and Rodney O. Fox</i>	159
Seismic Sounding of Convection in the Sun <i>Shravan Hanasoge, Laurent Gizon, and Katepalli R. Sreenivasan</i>	191
Cerebrospinal Fluid Mechanics and Its Coupling to Cerebrovascular Dynamics <i>Andreas A. Linninger, Kevin Tangen, Chih-Yang Hsu, and David Frim</i>	219
Fluid Mechanics of Heart Valves and Their Replacements <i>Fotis Sotiropoulos, Trung Bao Le, and Anvar Gilmanov</i>	259
Droplets and Bubbles in Microfluidic Devices <i>Shelley Lynn Anna</i>	285
Mechanics of Hydraulic Fractures <i>Emmanuel Detournay</i>	311
A Normal Mode Perspective of Intrinsic Ocean-Climate Variability <i>Henk Dijkstra</i>	341
Drop Impact on a Solid Surface <i>C. Josserand and S.T. Thoroddsen</i>	365

Contrail Modeling and Simulation <i>Roberto Paoli and Karim Shariff</i>	393
Modeling Nonequilibrium Gas Flow Based on Moment Equations <i>Manuel Torrilhon</i>	429
The Fluid Mechanics of Pyroclastic Density Currents <i>Josef Dufek</i>	459
The Dynamics of Microtubule/Motor-Protein Assemblies in Biology and Physics <i>Michael J. Shelley</i>	487
Dynamics and Instabilities of Vortex Pairs <i>Thomas Leweke, Stéphane Le Dizès, and Charles H.K. Williamson</i>	507

Indexes

Cumulative Index of Contributing Authors, Volumes 1–48	543
Cumulative Index of Article Titles, Volumes 1–48	553

Errata

An online log of corrections to *Annual Review of Fluid Mechanics* articles may be found at <http://www.annualreviews.org/errata/fluid>